

**Beyond modelocking: High repetition-rate frequency  
combs derived from a continuous-wave laser**

by

**Daniel C. Cole**

B.S., Washington University in St. Louis, 2012

M.S., University of Colorado, 2015

A thesis submitted to the  
Faculty of the Graduate School of the  
University of Colorado in partial fulfillment  
of the requirements for the degree of  
Doctor of Philosophy  
Department of Physics

2018

This thesis entitled:  
Beyond modelocking: High repetition-rate frequency combs derived from a continuous-wave laser  
written by Daniel C. Cole  
has been approved for the Department of Physics

---

Reader1

---

Reader2

Date \_\_\_\_\_

The final copy of this thesis has been examined by the signatories, and we find that both the content and the form meet acceptable presentation standards of scholarly work in the above mentioned discipline.

Cole, Daniel C. (Ph.D., Physics)

Beyond modelocking: High repetition-rate frequency combs derived from a continuous-wave laser

Thesis directed by Dr. Scott A. Diddams

Optical frequency combs based on modelocked lasers have revolutionized precision metrology by facilitating measurements of optical frequencies, with implications both for fundamental scientific questions and for applications such as fast, broadband spectroscopy. In this thesis, I describe advances in the generation of frequency combs without modelocking in platforms with smaller footprints and higher repetition rates, with the ultimate goal of bringing frequency combs to new applications in a chip-integrated package. I discuss two approaches for comb generation: parametric frequency conversion in Kerr microresonators and active electro-optic modulation of a continuous-wave laser. After introducing microresonator-based frequency combs (microcombs), I discuss two specific developments in microcomb technology: First, I describe a new, extremely reliable method for generation of soliton pulses through the use of a phase-modulated pump laser. This technique eliminates the dependence on initial conditions that was formerly a universal feature of these experiments, presenting a solution to a significant technical barrier to the practical application of microcombs. Second, I present observations of soliton crystal states with highly structured fingerprint optical spectra that correspond to ordered pulse trains exhibiting crystallographic defects. These pulse trains arise through interaction of solitons with avoided mode-crossings in the resonator spectrum. I also discuss generation of Kerr soliton combs in the Fabry-Perot (FP) geometry, with a focus on the differences between the FP geometry and the ring geometry that has been the choice of most experimenters to date. Next, I discuss combs based on electro-optic modulation. I introduce the operational principle, and then describe the first self-referencing of a frequency comb of this kind and a proof-of-principle metrology experiment. Finally, I discuss a technique for reducing the repetition rate of a high-repetition-rate frequency comb, which will be a necessary post-processing step for some applications. I conclude with a discussion of avenues for future research.

## Contents

<b>1</b>	<b>Introduction to microresonator-based frequency combs</b>	<b>1</b>
1.1	Optical microring resonators . . . . .	2
1.1.1	Resonant enhancement in a microring resonator . . . . .	4
1.1.2	Thermal effects in microresonators . . . . .	6
1.2	Microring resonator Kerr frequency combs . . . . .	8
1.2.1	A model for Kerr-comb nonlinear optics: The Lugiato-Lefever equation . . . . .	10
1.3	Description of Kerr-comb outputs using the Lugiato-Lefever equation . . . . .	13
1.3.1	Analytical investigation of the resonator's CW response . . . . .	13
1.3.2	Kerr comb outputs: extended modulation-instability patterns . . . . .	17
1.3.3	Kerr comb outputs: solitons . . . . .	19
<b>2</b>	<b>Downsampling of optical pulse trains</b>	<b>27</b>
2.1	Proof-of-Concept Experiment . . . . .	28
2.2	Mathematical model for downsampling . . . . .	29
2.3	Experimental investigation of the effect of downsampling on the pulse train's noise properties . . . . .	31
2.4	Effects of ideal downsampling on a pulse train's noise properties . . . . .	34
2.5	Model for the effect of incomplete extinction of rejected pulses and amplification of a downsampled pulse train . . . . .	36
2.6	Further remarks on the application of downsampling . . . . .	39

<b>A</b>	<b>Numerical simulations of nonlinear optics</b>	<b>42</b>
A.1	RK4IP algorithm . . . . .	42
A.2	Adaptive step-size algorithm . . . . .	43
A.3	Pseudocode for numerical simulation with the RK4IP algorithm and adaptive step size	44
A.3.1	Simulation of the LLE . . . . .	45
A.3.2	Simulation of the GNLSE . . . . .	46
	<b>References</b>	<b>47</b>

## Figures

1.1	Optical microdisk resonator . . . . .	3
1.2	Thermal bistability in microresonators . . . . .	8
1.3	An illustration of four-wave mixing and frequency-comb generation. . . . .	9
1.4	Solution space for the Lugiato-Lefever equation . . . . .	14
1.5	Investigation of the circulating CW power in a Kerr resonator . . . . .	15
1.6	Extended-pattern solutions to the LLE . . . . .	18
1.7	Soliton solutions to the LLE . . . . .	21
1.8	Kerr-soliton energy-level diagram . . . . .	24
2.1	An illustration of pulse-train repetition-rate downsampling . . . . .	28
2.2	Demonstration of downsampling for $f_0$ detection . . . . .	30
2.3	Experimental investigation of noise introduced by downsampling . . . . .	32
2.4	Effect of downsampling on photocurrent fluctuations . . . . .	37
2.5	Investigation of incomplete pulse extinction and amplification . . . . .	40

## Chapter 1

### Introduction to microresonator-based frequency combs

This chapter introduces the basic physics of optical frequency-comb generation in Kerr-nonlinear microring resonators, with a particular emphasis on providing context for the results described in the subsequent chapters. This field emerged in 2007 with the first report of comb generation in silica microtoroids [1], and has evolved rapidly. There are facets to the field that are not discussed here; we note that a number of papers that review this topic have been published, each of which provides a unique perspective [2–5]. The combs generated in Kerr-nonlinear ring resonators, excluding those generated in definitively ‘macro’ fiber loops, have generally been called microcombs, despite the fact that some of the resonators used to generate them have dimensions on the scale of several millimeters. Microcombs are an attractive technology because of their high repetition rates and small footprints, especially relative to modelocked-laser-based combs, which make them promising candidates for inclusion in integrated photonics systems. Microcomb generation has been reported in a variety of platforms, including the aforementioned silica microtoroids, silica wedge [6, 7] and rod [8] resonators, crystalline magnesium-fluoride [9] and calcium-fluoride [10] resonators, and silicon-nitride waveguide resonators [11, 12], which have the advantage of being immediately amenable to photonic integration.

For simplicity, and following the terminology of the field, we will refer to broadband optical spectra generated through frequency conversion in Kerr-nonlinear microring resonators as ‘Kerr combs,’ even when the output is not strictly a coherent frequency comb. Finally, we note that although researchers have so far focused on Kerr-comb generation with the ring geometry, is also

possible to generate Kerr combs in a Kerr-nonlinear Fabry-Perot (FP) cavity, as has been demonstrated in several experiments [13, 14]. Theoretical investigations of Kerr-comb generation with the FP geometry are presented in Chapter ??.

## 1.1 Optical microring resonators

An optical microring resonator guides light for many round trips around a closed path in a dielectric medium by total internal reflection. The principle is the same as the guiding of light in an optical fiber, and indeed a ‘macroring’ resonator can be constructed from a loop of fiber, using a fiber-optic coupler with a small coupling ratio as an input/output port. Microring resonators can be constructed by looping an optical waveguide back on itself, in which case the resonator provides index contrast and light confinement over a full  $360^\circ$  of the modal cross-section. Alternatively, resonators can be realized with geometries that lack an inner radius dimension and therefore provide less spatial confinement. In this case they can host ‘whispering-gallery modes,’<sup>1</sup> so-called due to their similarity with the acoustic ‘whispering-gallery’ waves that permit a listener on one side of St. Paul’s cathedral (for example) to hear whispers uttered by a speaker on the other side of the cathedral. A schematic depiction of the basic components of a typical microring-resonator experiment is shown in Fig. 1.1. Optical microring resonators have a host of characteristics that make them useful for photonics applications in general and for nonlinear optics in particular; these include the ease with which they can be integrated and the ability to tailor the spectral distribution of guided modes through careful resonator design, as well as the ultra-high quality factors that have been demonstrated ( $\geq$  several hundred million). The resonator quality factor  $Q$  is defined as  $Q = \omega_0 \tau_{ph} = \nu_0 / \Delta\nu$ , where  $\omega_0 = 2\pi\nu_0$  is the optical angular frequency,  $\tau_{ph}$  is the photon lifetime, and  $\Delta\nu$  is the resonance linewidth. The  $Q$  can be interpreted literally as the optical phase that is traversed by the carrier wave during the photon lifetime and is a useful figure of merit for nonlinear optics.

---

<sup>1</sup> In some sources the terminology ‘whispering-gallery mode resonator’ has been applied more generally, but the analogy to the acoustic case seems most appropriate for resonators in which index contrast is not provided over a full  $360^\circ$  of the modal cross-section. Otherwise it is unclear what makes a WGM resonator different from a fiber loop, which in the limit of large radius obviously does not host whispering-gallery modes. This issue of terminology is discussed in Ref. [15].



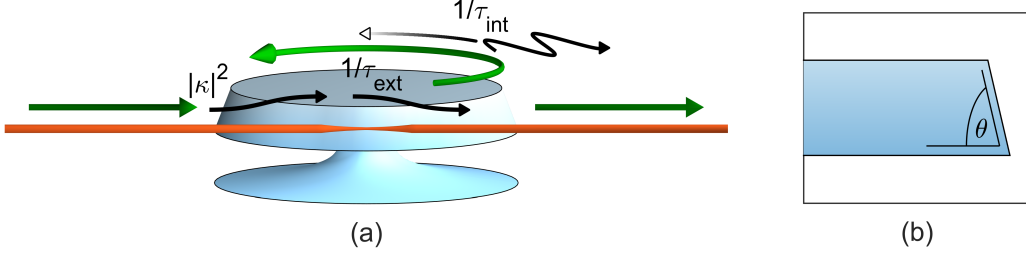


Figure 1.1: **Optical microdisk resonator.** (a) An optical microring resonator with the disk geometry as described in Ref. [6], operated in a through-coupled configuration. Light (green) is evanescently coupled into and out of the resonator through a tapered optical fiber, shown in orange, which contacts the resonator near the fiber's point of smallest diameter. Light circulates in whispering-gallery modes concentric to the resonator's circumference. The black labels indicate the coupling and loss rates discussed in Sec. 1.1.1:  $|\kappa|^2$  is the rate at which incoming photons are coupled into the resonator,  $1/\tau_{ext}$  is the rate at which circulating photons are coupling into the waveguide, and  $1/\tau_{int}$  is the intrinsic loss rate. Here contributions to  $1/\tau_{int}$  from absorption and radiative losses are depicted. (b) The wedge angle  $\theta$  can be adjusted to control the geometric dispersion of the propagating whispering-gallery modes as described in Ref. [16], as  $\theta$  dictates, for example, the extent to which larger (longer-wavelength) modes are confined further from the circumference of the wedge.

A microring resonator supports propagating guided modes of electromagnetic radiation with (vacuum) wavelengths that evenly divide the optical round-trip path length:  $\lambda_m = n_{eff}(\lambda_m)L/m$ , with associated resonance frequencies  $\nu_m = c/\lambda_m = mc/n_{eff}(\nu_m)L$ . This leads to constructive interference from round trip to round trip. Here  $m$  is the azimuthal mode number and the quantity  $Ln_{eff}(\lambda_m)$  is the optical round-trip path length of the mode, where  $n_{eff}(\lambda_m)$  defines an effective index of refraction related to the mode's propagation constant  $\beta_{prop}(\omega)$  via  $\beta_{prop}(\omega) = n_{eff}(\omega)\omega/c$  (see e.g. Refs. [17, 18]; we use the subscript *prop* to remove ambiguities arising from the standard use of the symbol  $\beta$  for multiple quantities). The free-spectral range  $f_{FSR}$  of a resonator is the *local* frequency spacing between modes, calculated via:

$$f_{FSR} \approx \frac{\nu_{m+1} - \nu_{m-1}}{2} \quad (1.1)$$

$$= \frac{\partial \nu_m}{\partial m} \quad (1.2)$$

$$= \frac{c}{n_{eff}(\nu)L} - \frac{mc}{n_{eff}^2(\nu)L} \frac{\partial n_{eff}}{\partial \nu} \frac{\partial \nu}{\partial m}, \quad (1.3)$$

so that, rearranging, we obtain:

$$f_{FSR} = \frac{c/L}{\left(n_{eff} + \nu \frac{\partial n_{eff}}{\partial \nu}\right)} = \frac{c}{n_g L} = 1/T_{RT}, \quad (1.4)$$

where  $n_g = n_{eff} + \nu \frac{\partial n_{eff}}{\partial \nu}$  is the group velocity of the mode and  $T_{RT}$  is the mode's round-trip time. The effective index  $n_{eff}$  is frequency dependent due to both intrinsic material dispersion and geometric dispersion, where the latter results for example from different sampling of material properties for different wavelength-dependent mode areas. A frequency-dependent  $n_{eff}$  leads to a non-uniform spacing in the cavity modes in frequency despite the linearity of  $\nu_m$  in  $m$ ; equivalently this results in a frequency dependence of  $n_g$  and  $f_{FSR}$ .

Depending on the design, microring resonators can support many transverse mode profiles, or just one. The former is typical of whispering-gallery-mode resonators that lack an inner radius, such as the wedge resonator shown in Fig. 1.1 or free-standing silica microrod resonators [8]; the latter can be readily achieved using chip-integrated single-mode photonic waveguides. For a given resonator geometry, to calculate the frequency-dependent effective index  $n_{eff}(\nu)$ , thereby enabling calculation of the resonance frequencies and wavelengths, one must solve Maxwell's equations for the resonator geometry. Except in special cases of high symmetry (e.g. a dielectric sphere [19]), this is typically done numerically using finite-element modeling tools like COMSOL. The modes of an optical resonator, both within a mode family defined by a transverse mode profile (such that they differ only by azimuthal mode number  $m$ ) and between mode families, must be orthogonal [20], with no linear coupling between them.

### 1.1.1 Resonant enhancement in a microring resonator

The lifetime  $\tau_{ph}$  of circulating photons in a resonator is fundamental to its fitness for applications. Generally, two processes lead to the loss of circulating photons: intrinsic dissipation that occurs at a rate  $1/\tau_{int}$  and out-coupling to an external waveguide that occurs at a rate  $1/\tau_{ext}$ , leading to a total loss rate of  $\tau_{ph}^{-1} = \tau_{ext}^{-1} + \tau_{int}^{-1}$ . To understand the quantitative role of these parameters, we consider a cavity mode of frequency  $\omega_0$  and described by instantaneous amplitude  $a(t)$  (normalized

such that  $|a|^2 = N$ , the number of circulating photons) driven by a pump field with frequency  $\omega_p$  and rotating amplitude  $s \propto \exp(i\omega_p t)$  (normalized such that  $|s|^2 = S$ , the rate at which photons in the coupling waveguide pass the coupling port) that is in-coupled with strength  $\kappa$ . The equation of motion for such a system is [20]:

$$\frac{da}{dt} = i\omega_0 a - \left( \frac{1}{2\tau_{int}} + \frac{1}{2\tau_{ext}} \right) a + \kappa s, \quad (1.5)$$

and the rates that determine the evolution of  $a$  are shown schematically in Fig. 1.1. We can immediately solve this equation by assuming that  $a \propto \exp(i\omega_p t)$ , and we obtain:

$$a = \frac{\kappa s}{\left( \frac{1}{2\tau_{int}} + \frac{1}{2\tau_{ext}} \right) + i(\omega_p - \omega_0)}. \quad (1.6)$$

The coupling strength  $\kappa$  into the waveguide and the out-coupling rate  $1/\tau_{ext}$  are related by  $|\kappa|^2 = 1/\tau_{ext}$ ; one can arrive at this conclusion by considering the special case  $1/\tau_{int} = 0$  and exploiting the time-reversal symmetry of the system under this condition [20]. By squaring Eq. 1.6 and inserting this relationship between  $\kappa$  and  $\tau_{ext}$ , we find:

$$N = \frac{\Delta\omega_{ext} S}{\Delta\omega_{tot}^2/4 + (\omega_p - \omega_0)^2}, \quad (1.7)$$

where we have defined the rates  $\Delta\omega_{ext} = 1/\tau_{ext}$ ,  $\Delta\omega_{int} = 1/\tau_{int}$ , and  $\Delta\omega_{tot} = \Delta\omega_{ext} + \Delta\omega_{int}$ . Two important observations can be drawn from Eq. 1.7: First, the cavity response is Lorentzian with a full-width at half-maximum (FWHM) linewidth that is related to the photon lifetime via  $\tau_{ph} = 1/\Delta\omega_{tot}$ , and second, on resonance the number of circulating photons is related to the input rate by the factor  $\Delta\omega_{ext}/\Delta\omega_{tot}^2 \ll 1$ . This factor is not yet the resonant enhancement, which we now calculate by considering the circulating power  $P = N\hbar\omega_p/T_{RT}$  on resonance (when  $\omega_p = \omega_0$ ):

$$P = \frac{4\Delta\omega_{ext} P_{in}/T_{RT}}{\Delta\omega_{tot}^2}, \quad (1.8)$$

$$= \frac{2}{\pi} P_{in} \eta \mathcal{F}, \quad (1.9)$$

where  $\mathcal{F} = 2\pi\tau_{ph}/T_{RT} = f_{FSR}/\Delta\nu$  is the resonator finesse,  $\eta = \Delta\omega_{ext}/\Delta\omega_{tot}$  is the coupling ratio, typically of order  $\sim \frac{1}{2}$ , and  $P_{in} = \hbar\omega_p S$  is the power in the waveguide. Thus, the circulating power is approximately a factor  $\mathcal{F}$  greater than the input power. The combination of this resonant

enhancement and a small cavity mode volume enables very large circulating optical intensities in high finesse resonators, which is important for the application of microresonators in nonlinear optics.

### 1.1.2 Thermal effects in microresonators

In a typical microresonator frequency-comb experiment, a frequency-tunable pump laser is coupled evanescently into and out of the resonator using a tapered optical fiber [21, 22] (for e.g. free-standing silica disc resonators) or a bus waveguide (for chip-integrated resonators, e.g. in silicon nitride rings). When spatial overlap and phase-matching ( $n_{eff,res} \sim n_{eff,coupler}$  [23]) between the evanescent mode of the coupler and a whispering-gallery mode of the resonator is achieved, with the frequency of the pump laser close to the resonant frequency of that mode, light will build up in the resonator and the transmission of the pump laser past the resonator will decrease.

In any experiment in which a significant amount of pump light is coupled into a resonator, one immediately observes that the cavity resonance lineshape in a scan of the pump-laser frequency is not Lorentzian as expected from Eq. 1.7; plots of measured resonance lineshapes are shown in Fig. 1.2a. This is because the resonator heats as it absorbs circulating optical power. Associated with this change in temperature are changes in the mode volume and the refractive index, described respectively by the coefficient of thermal expansion  $\partial V/\partial T$  and the thermo-optic coefficient  $\partial n/\partial T$ . For typical microresonator materials the thermo-optic effect dominates, and  $\partial n/\partial T > 0$  leads to a decrease in the resonance frequency with increased circulating power in thermal steady state. Thus, for an adiabatic scan across the cavity resonance with decreasing laser frequency, as the laser approaches the resonance in frequency space and power is coupled into the resonator, the resonance frequency will begin to shift with the laser frequency, and a sawtooth-shaped resonance emerges.

The thermal dynamics related to  $\partial n/\partial T$  and  $\partial V/\partial T$  dictate the signs and values of detuning  $\omega_0 - \omega_p$  that are readily accessible in experiment. Specifically, a calculation of the thermal dynamics of the system composed of the pump laser and the resonator reveals that when the pump laser with frequency  $\omega_p$  is near the ‘cold-cavity’ resonance frequency of a given cavity mode  $\omega_{0,cold}$  the resonance has three possible thermally-shifted resonance frequencies  $\omega_{0,shifted}$  at which thermal steady state

is achieved [24]. Generally, these points are:

- (1)  $\omega_p > \omega_{0,shifted}$ , blue detuning<sup>2</sup> with significant coupled power and thermal shift
- (2)  $\omega_p < \omega_{0,shifted}$ , red detuning with significant coupled power and thermal shift
- (3)  $\omega_p \ll \omega_0$ , red detuning with insignificant coupled power and insignificant thermal shift

These points are depicted schematically in Fig. 1.2b. Steady-state point (1) is experimentally important, because in the presence of pump-laser frequency and power fluctuations it leads to so-called thermal ‘self-locking.’ Specifically for steady-state point (1), this can be seen as follows:

- If the pump-laser power increases, the cavity heats, the resonance frequency decreases, the detuning increases, and the change in coupled power is minimized.
- If the pump-laser power decreases, the cavity cools, the resonance frequency increases, the detuning decreases, and the change in coupled power is minimized.
- If the pump-laser frequency increases, the cavity cools, the resonance frequency increases, and the change in coupled power is minimized.
- If the pump-laser frequency decreases, the cavity heats, the resonance frequency decreases, and the change in coupled power is minimized.

This is in contrast with steady-state point (2), where each of the four pump-laser fluctuations considered above generates a positive feedback loop, with the result that any fluctuation will push the system towards point (1) or point (3) and so point (2) is unstable. This preference of the system to occupy point (1) or point (3) over a range of pump-laser detuning is referred to as thermal bistability. As a result of this bistability, point (2) (i.e. red detuning with significant coupled power) cannot be observed in an experimental scan of the pump laser across the resonance in either direction. As explained above, when the pump-laser frequency is decreased the resonance takes on a broad sawtooth shape, while in an increasing-frequency scan the resonance takes on a narrow

---

<sup>2</sup> Here we use the convention that the ‘color’ of the detuning specifies the position of the laser with respect to the resonance—‘blue’ detuning means that the laser is more blue, or higher in frequency.

pseudo-Lorentzian profile whose exact shape depends on the scan parameters relative to the thermal timescale. A second consequence is that, in the absence of other stabilizing effects, operation at red detuning with significant coupled power in a microresonator experiment requires special efforts to mitigate the effects of thermal instability.

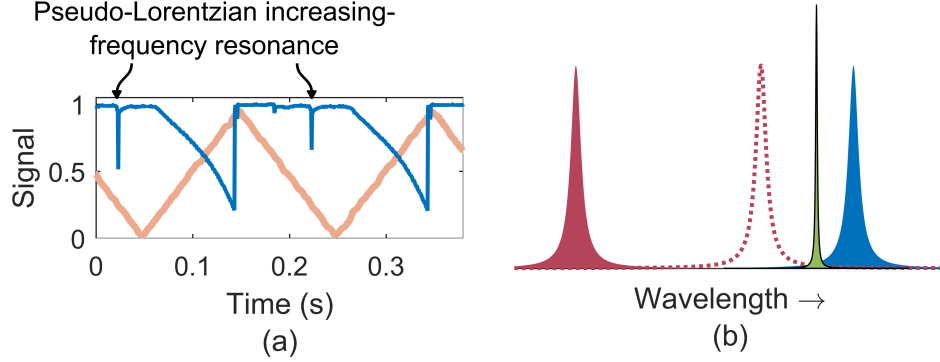


Figure 1.2: **Thermal bistability in microresonators.** (a) Measurement of power transmitted past the microresonator (blue) in an experiment using a  $\sim 16.5$  GHz-FSR microdisk resonator and a tapered fiber. The wavelength of the pump laser is controlled by a piezo-electric crystal that adjusts the length of the laser cavity. Here, larger control signal (orange) corresponds to longer laser wavelength. As the laser wavelength is increased, the resonator heats and a sawtooth-shaped resonance is observed. Ultimately the resonator reaches a maximum temperature that depends on the pump power, and the laser then becomes red-detuned as the wavelength continues to increase; then the resonator rapidly cools and the resonance is lost. Shortly thereafter, the direction of the scan is reversed. As the resonator wavelength is decreased, the system will ‘flip’ from steady-state point (3) to steady-state point (1), leading to observation of a narrow pseudo-Lorentzian resonance, with the exact shape depending on the thermal and scanning timescales. (b) Depiction of the three steady-state points for the laser detuning. For fixed laser wavelength (green), stable steady-state points exist with relatively small blue detuning and significant coupled power (solid blue), and relatively large red detuning and little coupled power (solid red). An unstable steady-state point also exists with red detuning and significant coupled power (dashed red). Note in this terminology that the color of the detuning (red or blue) refers to the position of the laser relative to the position of the resonance in wavelength space.

## 1.2 Microring resonator Kerr frequency combs

The high circulating optical intensities accessible in resonators with long photon lifetimes find immediate application in the use of microresonators for nonlinear optics. The experiments described in this thesis are conducted in silica microresonators. Silica falls into a broader class of materials that exhibit both centro-symmetry, which dictates that the second-order nonlinear susceptibility

$\chi^{(2)}$  must vanish, and a significant third-order susceptibility  $\chi^{(3)}$ . The  $n^{\text{th}}$ -order susceptibility is a term in the Taylor expansion describing the response of the medium's polarization to an external electric field [25]:  $P = P_0 + \epsilon_0\chi^{(1)}E + \epsilon_0\chi^{(2)}E^2 + \epsilon_0\chi^{(3)}E^3 + \dots$ . The effect of  $\chi^{(3)}$  can be described in a straightforward way as a dependence of the refractive index on the local intensity [17],

$$n = n_0 + n_2 I \quad (1.10)$$

where  $n_2 = \frac{3\chi^{(3)}}{4n_0^2\epsilon_0 c}$  is called the Kerr index [17, 26]. The intensity-dependence of the refractive index resulting from the third-order susceptibility  $\chi^{(3)}$  is referred to as the optical Kerr effect and enables the self-phase modulation, cross-phase modulation, and four-wave mixing (FWM) nonlinear processes, the last of which is depicted schematically in Fig. 1.3 [25].

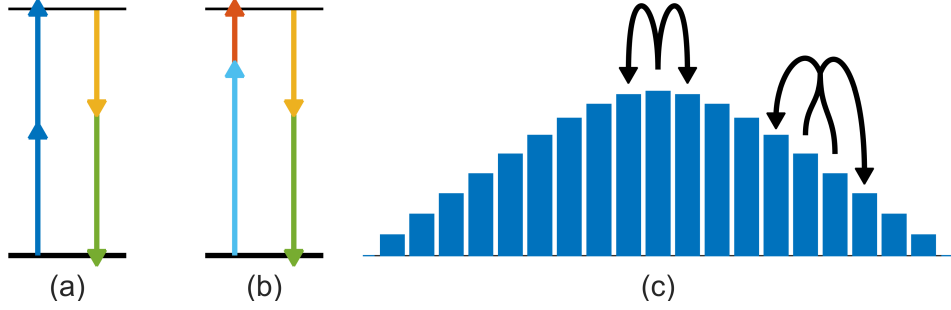


Figure 1.3: **An illustration of four-wave mixing and frequency-comb generation.** (a) Degenerate four-wave mixing, in which two fields of the same frequency  $\omega_1$  (blue) mix and generate fields at two new frequencies  $\omega'$  and  $\omega''$  (yellow and green). The schematic indicates the energy-conservation requirements of the process, which can be written as  $2\omega_1 = \omega' + \omega''$ . (b) Non-degenerate four-wave mixing, in which two fields of different frequencies  $\omega_2$  and  $\omega_3$  (light blue and orange) mix to generate fields at frequencies  $\omega'$  and  $\omega''$  (yellow and green). Energy conservation is now expressed as  $\omega_2 + \omega_3 = \omega' + \omega''$ . (c) Schematic depiction of one degenerate FWM step and one non-degenerate FWM step in a cascaded four-wave mixing process that generates a frequency comb. Figure after Ref. [2].

In 2007, a remarkable result brought about a new era for frequency comb research. Del'Haye et al. reported *cascaded four-wave mixing* (CFWM, shown in Fig. 1.3c) in anomalously-dispersive ( $\beta_{prop,2} = \frac{\partial^2 \beta_{prop}(\omega)}{\partial \omega^2} < 0$ ) toroidal silica microcavities on silicon chips, the result of which was a set of many co-circulating optical fields that were uniformly spaced by  $f_{rep}$  ranging from 375 GHz to  $\sim 750$  GHz (depending on the platform) [1]. This result built on previous demonstrations of few-mode parametric oscillation in microresonators [27–29], and showed that the non-uniform distribution of cavity resonance frequencies due to dispersion could be overcome to generate an output with

equidistant frequency modes. A second important development occurred in 2012, when Herr et al. reported the generation of frequency combs corresponding in the time domain to single circulating optical ‘soliton’ pulses [30, 31]. This observation followed the observation of solitons in formally-equivalent passive fiber-ring resonators in 2010 [32]. Due to unique properties that make them particularly well-suited for applications, as discussed in Sec. 1.3.3, the generation and manipulation of soliton combs has become a significant priority in microcomb research.

### 1.2.1 A model for Kerr-comb nonlinear optics: The Lugiato-Lefever equation

Kerr-comb generation can be motivated and partially understood through the CFWM picture [33], but the phase and amplitude degrees of freedom for each comb line mean that CFWM gives rise to a rich space of comb phenomena—it is now known that Kerr combs can exhibit several fundamentally distinct outputs. A useful model for understanding this rich space is the Lugiato-Lefever equation (LLE), which was shown to describe microcomb dynamics by Chembo and Menyuk [34] through Fourier-transformation of a set of coupled-mode equations describing CFWM and by Coen, Randle, Sylvestre, and Erkintalo [35] through time-averaging of a more formally-accurate model for a low-loss resonator (as first performed by Haelterman, Trillo, and Wabnitz [36]). The LLE is a nonlinear partial-differential equation that describes evolution of the normalized cavity field envelope  $\psi$  over a slow time  $\tau = t/2\tau_{ph}$  in a frame parametrized by the ring’s azimuthal angle  $\theta$  (running from  $-\pi$  to  $\pi$ ) co-moving at the group velocity.<sup>3</sup> The equation formulated by Chembo and Menyuk, as it will be used throughout this thesis, reads:

$$\frac{\partial \psi}{\partial \tau} = -(1 + i\alpha)\psi + i|\psi|^2\psi - i\frac{\beta_2}{2}\frac{\partial^2 \psi}{\partial \theta^2} + F. \quad (1.11)$$

This equation describes  $\psi$  over the domain  $-\pi \leq \theta \leq +\pi$  with periodic boundary conditions  $\psi(-\pi, \tau) = \psi(\pi, \tau)$ . Here  $F$  is the field strength of the pump laser, with  $F$  and  $\psi$  both normalized so that they take the value 1 at the absolute threshold for parametric oscillation:  $F = \sqrt{\frac{8g_0\Delta\omega_{ext}}{\Delta\omega_{tot}^3} \frac{P_{in}}{\hbar\omega_p}}$ ,  $|\psi|^2 = \frac{2g_0T_{RT}}{\hbar\omega_p\Delta\omega_{tot}} P_{circ}(\theta, \tau)$ , so that  $|\psi(\theta, \tau)|^2$  is the instantaneous normalized power at the co-moving

---

<sup>3</sup> The co-moving azimuthal angle  $\theta$  is analogous to the ‘fast time’ variable that appears in, for example, the nonlinear Schrodinger equation for fiber-optic pulse propagation [17], and it can be transformed explicitly to a fast time  $t$  via  $t = T_{RT} \times \frac{\theta}{2\pi}$ .



azimuthal angle  $\theta$ . Here  $g_0 = n_2 c \hbar \omega_p^2 / n_g^2 V_0$  is a parameter describing the four-wave mixing gain,  $\Delta\omega_{ext}$  is the rate of coupling at the input/output port,  $\Delta\omega_{tot} = 1/\tau_{ph}$  is the FWHM resonance linewidth,  $P_{in}$  is the pump-laser power,  $P_{circ}(\theta, \tau)$  is the local circulating power in the cavity,  $\hbar$  is Planck's constant, and  $\omega_p$  is the pump-laser frequency. The parameters  $n_2$ ,  $n_g$ , and  $V_0$  describe the nonlinear (Kerr) index (see Eqn. 1.10), the group index of the mode, and the effective nonlinear mode volume at the pump frequency;  $L$  is the physical round-trip length of the ring cavity.

The parameters  $\alpha$  and  $\beta_2$  describe the frequency detuning of the pump laser and second-order dispersion of the resonator mode family into which the pump laser is coupled, both normalized to half the cavity linewidth:

$$\alpha = -\frac{2(\omega_p - \omega_0)}{\Delta\omega_{tot}}, \quad (1.12)$$

$$\beta_2 = -\frac{2D_2}{\Delta\omega_{tot}}; \quad (1.13)$$

here  $D_2 = \left. \frac{\partial^2 \omega_\mu}{\partial \mu^2} \right|_{\mu=0}$  is the second-order modal dispersion parameter, where  $\mu$  is the pump-referenced mode number of Eq. ???. The parameters  $D_1 = \left. \frac{\partial \omega_\mu}{\partial \mu} \right|_{\mu=0} = 2\pi f_{FSR}$  and  $D_2$  are related to the derivatives of the propagation constant  $\beta_{prop} = n_{eff}(\omega)\omega/c$  via  $D_1 = 2\pi/L\beta_1$  and  $D_2 = -D_1^2 \frac{\beta_{prop,2}}{\beta_{prop,1}}$ , where  $\beta_{prop,n} = \partial^n \beta_{prop} / \partial \omega^n$ . The subscript *prop* is used here to distinguish the propagation constant from the LLE dispersion coefficients  $\beta_n = -2D_n/\Delta\omega_{tot}$ , as unfortunately the use of the symbol  $\beta$  for both of these quantities is standard. Expressions for higher-order modal dispersion parameters  $D_n$  in terms of the expansion of the propagation constant can be obtained by evaluating the equation  $D_{n>1} = (D_1 \frac{\partial}{\partial \omega})^{n-1} D_1$ , and may be incorporated into the LLE up to desired order  $N$  through the replacement:

$$-i \frac{\beta_2}{2} \frac{\partial^2 \psi}{\partial \theta^2} \rightarrow + \sum_{n=1}^N i^{n+1} \frac{\beta_n}{n!} \frac{\partial^n \psi}{\partial \theta^n}. \quad (1.14)$$

This thesis describes frequency-comb generation in anomalously-dispersive resonators, and so  $\beta_2 < 0$  throughout.

The formulation of the LLE in terms of dimensionless normalized parameters helps to elucidate the fundamental properties of the system and facilitates comparison of results obtained in platforms with widely different experimental conditions. The LLE relates the time-evolution of the intracavity

field (normalized to its threshold value for cascaded four-wave mixing) to the power of the pump laser (normalized to its value at the threshold for cascaded four-wave mixing), the pump-laser detuning (normalized to half the cavity linewidth), and the cavity second-order dispersion quantified by the change in the FSR per mode (normalized to half the cavity linewidth). One example of the utility of this formulation is that it makes apparent the significance of the cavity linewidth in determining the output comb, and underscores the fact that optimization of the dispersion, for example, without paying heed to the effect of this optimization on the cavity linewidth, may not yield the desired results. This adds an additional layer of complexity to dispersion engineering relative to straight waveguides.

The LLE is, of course, a simplified description of the dynamics occurring in the microresonator. It abstracts the nonlinear dynamics and generally successfully describes the various outputs that can be generated in a microresonator frequency comb experiment. The LLE is a good description of these nonlinear dynamics when the resonator photon lifetime, mode overlap, and nonlinear index  $n_2$  are roughly constant over the bandwidth of the generated comb, and when the dominant contribution to nonlinear dynamics is simply the self-phase modulation term  $i|\psi|^2\psi$  arising from the Kerr nonlinearity. The LLE neglects the polarization of the electric field ( $\psi$  is a scalar), as well as thermal effects and the Raman scattering and self-steepening nonlinearities, although in principle each of these can be included [17, 31, 37, 38]. It is also worth emphasizing that the LLE can be derived from a more formally-accurate Ikeda map (as explained by Coen et al. [35]), in which the effect of localized input- and output-coupling is included in the model. This derivation is accomplished by ‘delocalizing’ the pump field and the output-coupling over the round trip, including only their averaged effects. This is an approximation that is valid in the limit of high finesse due to the fact that the cavity field cannot change on the timescale of a single round trip, but as a result the LLE necessarily neglects all dynamics that might have some periodicity at the round-trip time; the fundamental timescale of LLE dynamics is the photon lifetime.

### 1.3 Description of Kerr-comb outputs using the Lugiato-Lefever equation

The LLE provides a useful framework for the prediction and interpretation of experimental results. Basically, it predicts the existence of two fundamentally distinct types of Kerr-combs: extended temporal patterns and localized soliton pulses. These predictions are born out by experiments, the interpretation of which is facilitated by insight gained from the LLE. In the remainder of this chapter I briefly present some analytical results that can be obtained from the LLE about the behavior of the continuous-wave (CW) field that exists in the resonator in the absence of Kerr-comb formation, and then discuss these two types of comb outputs. This discussion provides context for the results presented in the next two chapters. Fig. 1.4 summarizes the results that will be presented in the remainder of this chapter, and in particular shows the values of the parameters  $\alpha$  and  $F^2$  at which solitons and extended patterns can be obtained.

#### 1.3.1 Analytical investigation of the resonator's CW response

Some insight into comb dynamics can be obtained via analytical investigations of the LLE, Eq. 1.11. This section largely follows the analysis of Ref. [39], with similar analysis having been performed elsewhere, for example in Refs. [35] and [40]. When the derivative term  $\partial^2\psi/\partial\theta^2$  in the LLE is non-zero,  $\psi$  is necessarily broadband, and a Kerr comb has been formed. There are no known exact analytical solutions to the LLE to describe Kerr-comb outputs, which must instead be numerically simulated (see Appendix A). However, flat solutions  $\psi_{CW}$  to the LLE may be calculated by setting all derivatives to zero—when these solutions can be realized physically (discussed below), they describe a CW field in the resonator. Upon setting the derivatives in the LLE to zero, one finds:

$$F = (1 + i\alpha)\psi_{CW} - i|\psi_{CW}|^2\psi_{CW}. \quad (1.15)$$

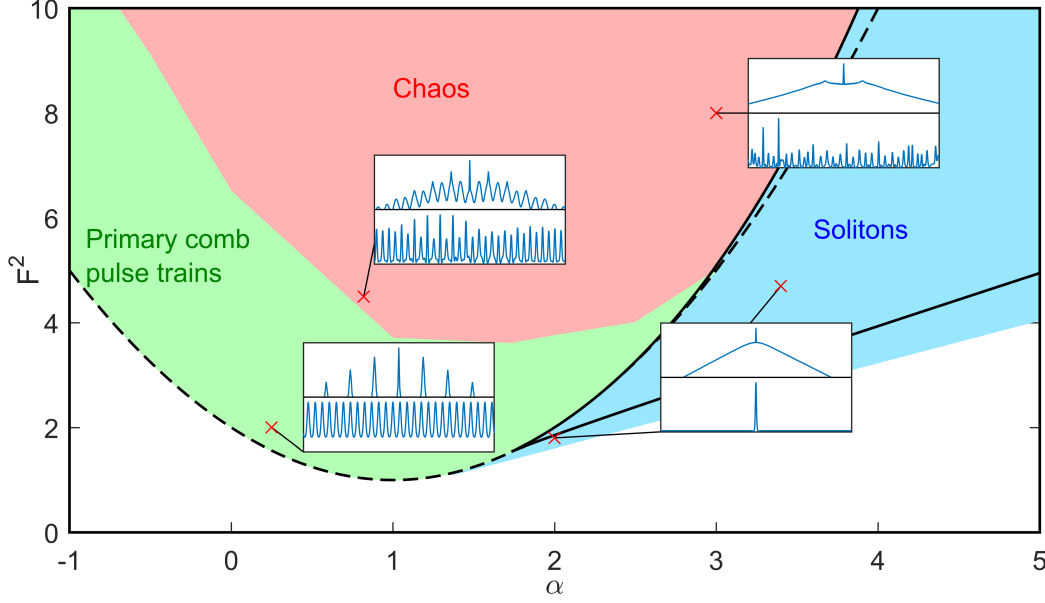


Figure 1.4: **Solution space for the Lugiato-Lefever equation.** Depiction of the various behaviors exhibited by  $\psi$  as a function of its position in the  $\alpha - F^2$  plane; this predicts the type of Kerr-comb output as a function of the pump-laser detuning and power, the parameters that are most readily adjusted in experiment. Curves plotted in black are obtained through analytical investigation of the LLE; these include the threshold curve for parametric oscillation (dashed black, Eq. 1.21) and the lines obtained via  $\rho(\alpha, F^2) = \rho_{\pm}(\alpha)$  (solid black, Eq. 1.18), which define the region where the LLE exhibits multiple flat solutions (i.e. solutions such that  $\partial\psi/\partial\theta = 0$ , Eq. 1.15). Extended patterns arise above the threshold curve through modulation instability. Solitons exist outside of the threshold curve at higher red detuning, up to an approximate maximum  $\alpha_{max} = \pi^2 F^2/8$ . The lines bounding the existence of chaos are not known precisely, and in fact chaos can be observed in simulation outside of the threshold curve at values  $\alpha > \alpha_{thresh,+}$  (Eq. 1.22). Insets show representative simulation results for the various types of comb outputs in the frequency (top) and time (bottom) domains. Fig. after Ref. [39].

The circulating intensity  $\rho = |\psi_{CW}|^2$  is obtained by taking the modulus-square of Eq. 1.15 to obtain:

$$F^2 = (1 + (\alpha - \rho)^2) \rho, \quad (1.16)$$

$$= \rho^3 - 2\alpha\rho^2 + (\alpha^2 + 1)\rho, \quad (1.17)$$

whereupon this equation can be numerically solved for  $\rho$ . As a third-order polynomial in  $\rho$  this equation has three solutions, one or three of which may be real; the complex solutions are unphysical. The function  $F^2(\alpha, \rho)$  defined by this equation uniquely determines  $F^2$  given  $\alpha$  and  $\rho$ . We now consider plotting a graph of  $F^2(\alpha, \rho)$  with  $\alpha$  held constant; examples are given in Fig. 1.5. By noting that  $F^2(\alpha, \rho = 0) = 0$  and  $\partial F^2/\partial\rho|_{\rho=0} > 0$ , we can conclude that a graph of  $F^2(\alpha, \rho)$  will cross the same value  $F^2$  three times if  $F^2$  is between the extremal values  $F^2_{\pm}(\alpha)$  at which  $\partial F^2/\partial\rho = 0$ .

This means that three real solutions  $\rho_1$ ,  $\rho_2$ , and  $\rho_3$  for the inverted function  $\rho(\alpha, F^2)$  exist for each value of  $F^2$  between  $F_-^2(\alpha)$  and  $F_+^2(\alpha)$ . The values  $F_\pm^2(\alpha)$  bounding this region of degeneracy in  $\rho$  are found by inserting the values  $\rho_\pm$  at which  $\partial F^2/\partial \rho = 0$  into Eq. 1.16. That is,  $F_\pm^2(\alpha) = F^2(\alpha, \rho_\mp)$ , where:

$$\rho_\pm = \frac{2\alpha \pm \sqrt{\alpha^2 - 3}}{3}. \quad (1.18)$$

For pump powers outside of the interval  $[F_-^2(\alpha), F_+^2(\alpha)]$ , which varies with  $\alpha$ , there is only one real solution  $\rho$ ; within this interval there are three. This is illustrated in Fig. 1.5. The smallest value of  $F^2$  at which the stationary curve  $\rho$  becomes multivalued is found to be  $F^2 = 8\sqrt{3}/9$  by solving for  $\rho_- = \rho_+$  and inserting the corresponding values into Eq. 1.16.

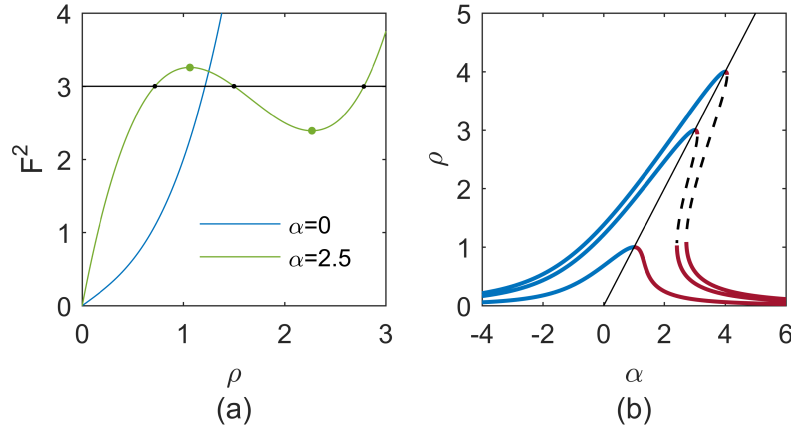


**Figure 1.5: Investigation of the circulating CW power in a Kerr resonator.** (a) Plots of  $F^2$  as a function of  $\rho$  for  $\alpha = 0$  (blue) and  $\alpha = 2.5$  (green), according to Eq. 1.16. When real values of  $\rho$  exist that extremize  $F^2$  according to this equation, multiple real solutions for the circulating power  $\rho$  exist between these extremal values of  $F^2$ . For  $\alpha = 2.5$  we indicate the extremal values of  $F^2$  as green dots. For an example value  $F^2 = 3$ , the corresponding allowed values  $\rho_1$ ,  $\rho_2$ , and  $\rho_3$  are the intersections of the green curve and the black line (black dots); such a line would have three intersections with the green curve for any value of  $F^2$  between  $F_\alpha^2(\rho_-)$  and  $F_\alpha^2(\rho_+)$ . (b) Kerr-tilted resonances curves  $\rho(\alpha)$  for  $F^2 = 1$  (smallest),  $F^2 = 3$ , and  $F^2 = 4$  (largest). The line  $\rho = \alpha = F^2$  (solid black) marks the highest circulating power for a given input power  $F^2$  and separates the effectively blue-detuned and effectively red-detuned branches. When  $F^2 > 8\sqrt{3}/9$  (obtained by solving for  $\rho_+ = \rho_-$ , Eq. 1.18), the resonance becomes tilted steeply enough that an unstable middle branch (dashed black) exists.

Physically, the coexistence of multiple flat solutions  $\rho$  at a given point  $(\alpha, F^2)$  corresponds to a ‘tilting’ of the Lorentzian transmission profile of the cavity and leads to bistability, even before taking into account thermal effects. This is illustrated in Fig. 1.5. For flat solutions  $\rho$ , an effective

Kerr-shifted detuning can be defined as  $\alpha_{eff} = \alpha - \rho$ . The effective detuning simply incorporates the Kerr nonlinearity into the round-trip phase shift that describes the constructive or destructive interference of the circulating field with the pump at the coupling port. By noting that  $\alpha = F^2 = \rho$  solves Eq. 1.16, we can conclude that the position of the effective Kerr-shifted resonance is on the line  $\alpha = F^2$ , where  $\alpha_{eff} = 0$ .

Once the circulating intensity  $\rho$  is known, the corresponding flat solution  $\psi_{CW}$  can be determined from Eq. 1.15 by inserting the known value of  $\rho$  and solving for  $\psi_{CW}$ , with the result:

$$\psi_{CW} = \frac{F}{1 + i(\alpha - \rho)}. \quad (1.19)$$

This expression reveals that the flat solution acquires a phase  $\phi_s = \tan^{-1}(\rho - \alpha)$  relative to the pump.

If the flat solution(s) at a point  $(\alpha, F^2)$  is (are) unstable, a Kerr comb will form spontaneously. Stability analysis of the flat solutions can be performed, and for the case of second-order dispersion alone the results are [39]:

- In the region of multi-stability, if the flat solutions are ordered with increasing magnitude as  $\rho_1$ ,  $\rho_2$ , and  $\rho_3$ , the middle solution  $\rho_2$  is always unstable.
- When  $\alpha < 2$ , a flat solution  $\rho$  that is not the middle solution is stable if  $\rho < 1$ ; otherwise it is unstable. When the flat solution is unstable, the mode that experiences the greatest instability has mode number given by:

$$\mu_{max} = \sqrt{\frac{2}{\beta_2}(\alpha - 2\rho)} \quad (1.20)$$

Therefore, the pump-laser threshold curve for Kerr-comb generation can be determined in the region  $\alpha < 2$  of the  $\alpha - F^2$  plane by setting  $\rho = 1$  in Eq. 1.15:

$$F_{thresh}^2 = 1 + (\alpha - 1)^2, \quad (1.21)$$

$$\alpha_{thresh,\pm} = 1 \pm \sqrt{F^2 - 1}. \quad (1.22)$$

These equations explicitly describe the point at which comb is generated in an experiment in which the pump power or detuning is varied while the other is held fixed.

### 1.3.2 Kerr comb outputs: extended modulation-instability patterns

Extended temporal patterns arise spontaneously as a result of the instability of the flat solution to the LLE when the pump laser is tuned above the threshold curve. Two types of extended patterns are shown in Fig. 1.6. These patterns can be stationary, in which case they are typically referred to as ‘Turing patterns’ or ‘primary comb,’ or can evolve in time, in which case they are typically referred to as ‘noisy comb’ or ‘spatiotemporal chaos.’ In general, the former occurs for lower values of the detuning  $\alpha$  and smaller pump strengths  $F^2$ ; although some studies of the transition from Turing patterns to chaos have been conducted (e.g. Ref. [41]), a well-defined boundary between the two has not been established, and may not exist.

In the spatial domain parametrized by  $\theta$ , a Turing pattern consists of a pulse train with (typically)  $n \gg 1$  pulses in the domain  $-\pi \leq \theta \leq \pi$ —the pulse train’s repetition rate is a multiple of the cavity FSR:  $f_{rep} = n \times f_{FSR}$ . Corresponding to the  $n$ -fold decreased period (relative to the round-trip time) of an  $n$ -pulse Turing pattern’s modulated waveform in the time domain, the optical spectrum of a Turing pattern consists of modes spaced by  $n$  resonator FSR—it is this widely-spaced spectrum that is referred to as ‘primary comb.’ Analytical approximations for Turing patterns are possible near threshold [42, 43] and in the small damping limit [44]. The stability analysis results from the last section can be used to predict the spacing  $n$  of a primary comb (equivalently the number of Turing-pattern pulses) generated in a decreasing-frequency scan across the resonance with fixed normalized pump power  $F^2$ :

$$n = \mu_{max,thresh} = \sqrt{\Delta\omega_0(1 + \sqrt{F^2 - 1})/D_2}, \quad (1.23)$$

which is obtained by inserting  $\alpha_{thresh,-}$  from Eq. 1.22 and  $\rho = 1$  into the expression for  $\mu_{max}$  in Eq. 1.20 above and moving to the dimensionful dispersion parameter  $D_2$ . Fig. 1.6a shows measured and simulated primary comb spectra and Fig. 1.6b shows the corresponding simulated time-domain waveform.

Spatiotemporal chaos can be understood as a Turing pattern whose pulses oscillate in height, with adjacent pulses oscillating out of phase. From such an oscillating Turing pattern, if  $\alpha$  and/or

$F^2$  is increased, one moves deeper into the chaotic regime and pulses begin to exhibit lateral motion and collisions; the number of pulses present in the cavity is no longer constant in time. Depending on the severity of the chaos (greater for larger  $\alpha$  and  $F^2$ ), a chaotic comb may correspond to a primary-comb-type spectrum with each primary-comb mode exhibiting sidebands at the resonator FSR, so-called ‘subcombs,’ or it may correspond to a spectrum with light in each cavity mode. Fig. 1.6c shows measured and simulated time-averaged spectra of chaotic combs and Fig. 1.6d shows a corresponding simulated time-domain waveform.

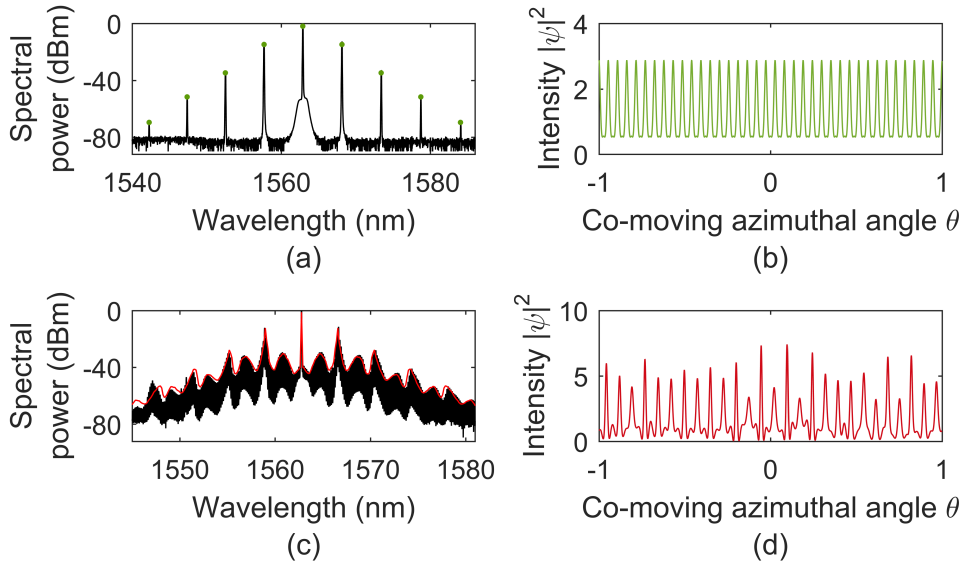


Figure 1.6: **Extended-pattern solutions to the LLE.** (a,b) Primary-comb pulse train in the frequency (a) and time (b) domains. The primary-comb spectrum corresponds to 39 time-domain pulses. The experimental optical spectrum (black) was obtained in a microdisk resonator with 17.32 GHz free-spectral range, and the simulation (green) is conducted with parameters near typical experimental values:  $F^2=6$ ,  $\alpha = -0.6$ , and  $\beta_2 = -0.0044$ . (c,d) Spatiotemporal chaos obtained in the same resonator. The experimental measurement (black) yields a time-averaged optical spectrum, with a simulation of qualitatively similar dynamics shown in red. Simulation parameters are  $F^2 = 4.2$ ,  $\alpha = 1.2$ , and  $\beta_2 = -0.0054$ . A snapshot of the evolving time-domain waveform is shown in (d).

Relative to generation of solitons, discussed below, experimental generation of an extended pattern is straightforward. These patterns are generated with blue effective pump-laser detuning  $\alpha_{eff} < 0$ , where thermal locking can occur. Because they arise spontaneously from noise, their generation is (comparatively) straightforward: simply decrease the pump-laser frequency until a



pattern is generated. Unfortunately, operation of a Kerr-comb in the extended pattern regime is disadvantageous for applications: the  $n$ -FSR spacing of primary comb presents a challenge for measurement of the repetition rate of the frequency comb due to the bandwidth of measurement electronics and is also an inefficient use of physical space (i.e. for an  $n$ -pulse primary comb pulse train, an equivalent pulse train can always be obtained using the single-soliton output of a resonator with area that is smaller by a factor of  $1/n^2$ ), and the aperiodic time-evolution of chaotic comb corresponds to modulation sidebands on the comb modes within the linewidth of the cavity that preclude the use of the comb as a set of stable optical reference frequencies.

An important property of these extended patterns is that they fill the resonator—the characteristic size of temporal features scales roughly as  $1/\sqrt{-\beta_2}$ , but these features are distributed densely and uniformly throughout the resonator. This means that the total circulating power of an extended pattern  $\int d\theta |\psi|^2$  is large relative to the localized pulses discussed in the next section, and therefore that extended patterns come with a comparatively large thermal shift of the resonance. As explained below, this contributes to the experimental challenges in soliton generation.

### 1.3.3 Kerr comb outputs: solitons

The term ‘soliton’ generally refers to a localized excitation that can propagate without changing its shape due to a delicate balance between dispersion (or diffraction) and nonlinearity; sometimes known as ‘solitary waves,’ solitons entered the scientific consciousness in the nineteenth century with their observation by John Scott Russell [45]. They are fundamental solutions to nonlinear partial-differential equations that describe a host of physical phenomena, and are found in several contexts within the field of nonlinear optics: spatial[42, 46] and spatiotemporal solitons (light bullets) [47] have been studied, and soliton modelocking [48, 49] is an important method of femtosecond pulse generation. Temporal Kerr-soliton pulses in optical fibers are particularly well known [17, 50], and have been considered as a candidate for fiber-optic communications protocols [51, 52]. Microresonators support so-called dissipative cavity solitons, which are localized pulses circulating the resonator that are out-coupled once per round trip. In the case of a single circulating soliton,

this leads to a train of pulses propagating away from the resonator with repetition rate  $1/T_{RT}$ . Thus the mode spacing of the comb matches the FSR of the resonator, in contrast with widely-spaced primary comb spectra, and the soliton can, in principle, remain stable and propagate indefinitely as a stationary solution to the LLE. This makes Kerr combs based on solitons particularly attractive for applications.

### 1.3.3.1 Mathematical description of solitons

Solitons in optical fibers are solutions of the nonlinear Schrodinger equation (NLSE) that describes pulse-propagation in optical fiber [17]:

$$\frac{\partial A}{\partial z} = i\gamma|A|^2 A - i\frac{\beta}{2} \frac{\partial^2 A}{\partial T^2}. \quad (1.24)$$

This equation describes the evolution of the pulse envelope  $A$  in the ‘fast-time’ reference frame parametrized by  $T$  as it propagates down the length of the fiber, parametrized by the distance variable  $z$ . Here  $\gamma = \frac{2\pi}{\lambda} \frac{n_2}{A_{eff}}$  is the nonlinear coefficient of the fiber, where  $n_2$  is the Kerr index,  $A_{eff}$  is the effective nonlinear mode area and  $\lambda$  is the carrier wavelength, and  $\beta \equiv \beta_{prop,2}$  is the GVD parameter. The LLE can be viewed as an NLSE with additional loss and detuning terms  $-(1+i\alpha)\psi$  and a driving term  $F$ .

The fundamental soliton solution to the NLSE is:

$$A_{sol} = \sqrt{P_0} \operatorname{sech}(T/\tau) e^{i\gamma P_0 z/2 + i\phi_0}, \quad (1.25)$$

where  $P_0$  is the peak power of the pulse and is related to the duration of the pulse  $\tau$  via  $\tau = \sqrt{-\beta/\gamma P_0}$ , and  $\phi_0$  is an arbitrary phase. Thus, this equation admits a *continuum* of pulsed fundamental ‘soliton’ solutions, with one existing for each value of the peak power. Each of these solutions propagates down the fiber without changing shape; only the phase evolves with distance as  $\phi(z) = \gamma P_0 z/2 + \phi_0$ .

The introduction of the loss, detuning, and driving terms into the NLSE to obtain the LLE has several important consequences for solitons. First, exact analytical expressions for the soliton solution to the LLE in terms of elementary functions are not known, in contrast with the situation

for the NLSE. However, the soliton solutions to the LLE, Eq. 1.11, can be approximated well as:

$$\psi_{sol} = \psi_{CW,min} + e^{i\phi_0} \sqrt{2\alpha} \operatorname{sech} \sqrt{\frac{2\alpha}{-\beta_2}} \theta. \quad (1.26)$$

Here  $\psi_{CW,min}$  is the flat solution to the LLE from Eq. 1.19 at the point where the soliton solution is desired; when multiple flat solutions exist,  $\psi_{CW,min}$  is the one corresponding to the smallest intensity  $\rho_1$ . The phase  $\phi_0 = \cos^{-1}(\sqrt{8\alpha}/\pi F)$  arises from the intensity-dependent phase shift in the cavity due to the Kerr effect, mathematically described by the term  $i|\psi|^2\psi$ . We depict this approximation, alongside numerical calculations of exact soliton solutions to the LLE, in Fig. 1.7.

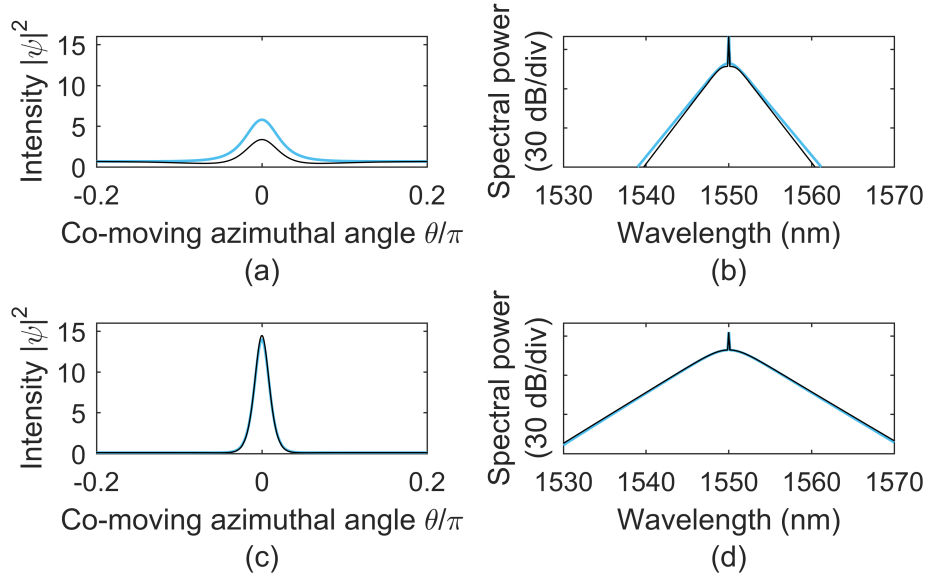


Figure 1.7: **Soliton solutions to the LLE.** Analytical approximations (color) and numerically-calculated exact solutions (black) to the LLE in the time (a,c) and frequency (b,d) domains. The solitons are calculated at  $\alpha = 0.95 \alpha_{max} = 0.95 \pi^2 F^2 / 8$  for  $F^2 = 8\sqrt{3}/9$  (a,b) and  $F^2 = 6$  (c,d) with  $\beta_2 = -0.02$  in both cases. The isolated spectral spike is at the pump frequency and corresponds to the CW background  $\psi_{CW,min}$ . Spectra are calculated using  $f_{rep} = 16.5$  GHz with pump wavelength of  $\lambda_p = 1550$  nm. For experimental measurements of solitons in microring resonators, see Chapters ?? and ??.

This approximation  $\psi_{sol}$  from Eq. 1.26 for the soliton solution of the LLE illustrates a second important consequence of the differences between the NLSE and the LLE: while the NLSE admits a continuum of fundamental soliton solutions parametrized by their peak power  $P_0$  and arbitrary phase  $\phi_0$ , the LLE supports only one shape for the envelope of a soliton for fixed experimental parameters.

Intuitively, this can be understood as arising from the need for the round-trip phase shift for all points on the soliton to be zero in steady-state; the introduction of the detuning parameter  $\alpha$  breaks the degeneracy that exists for the NLSE within the continuum of soliton solutions.

The analytical approximation in Eq. 1.26 indicates the scaling of the amplitude and width of the LLE soliton with the experimental parameters: the amplitude of the LLE soliton, prior to its summation with the CW background, depends only on the detuning  $\alpha$ , and the width of the soliton increases with larger detuning  $\alpha$  and smaller dispersion  $\beta_2$ . Importantly, if one is concerned with maximizing the bandwidth of the soliton, it is important to minimize  $\beta_2$  and maximize  $\alpha$ , due to the inverse relationship between temporal duration and spectral bandwidth. The spectrum of a single-soliton Kerr comb has a  $\text{sech}^2((\omega - \omega_p)/\Delta\omega_{sol})$  envelope, where  $\omega$  is the optical angular frequency and  $\Delta\omega_{sol} \approx \sqrt{32\alpha/|\beta_2|T_{RT}^2}$  is the bandwidth of the pulse in angular frequency. Equivalently, the bandwidth of the soliton in (linear) optical frequency is  $\sqrt{\frac{16\Delta\nu f_{rep}^2}{D_2}}\alpha$ , where  $\Delta\nu$  is the resonance linewidth in linear frequency; the spectral width in mode number is  $\Delta\mu_{sol} \approx 4\sqrt{\alpha\Delta\nu/D_2}$ . Consistent with the phase  $\phi_0$  in the approximation  $\psi_{sol}$  in Eq. 1.26, solitons can exist up to a maximum detuning of  $\alpha_{max} \sim \pi^2 F^2/8$  [31]. For a soliton at the maximum detuning for fixed normalized pump power  $F^2$ , the bandwidth is then  $\sqrt{\frac{\pi^2\Delta\nu f_{rep}^2}{2D_2}F^2}$ .

Solitons exist only where there is a stable flat solution  $\psi_{CW}$  that is effectively red detuned that can form the background for the pulse [40, 53]. This effectively red-detuned background is itself thermally unstable (see Sec. 1.1.2), but the existence of the soliton acts to stabilize the pump detuning. As explained by Herr et al., the soliton provides a local modulation of the refractive index through the Kerr effect, which changes the round-trip phase shift of pump light that arrives coincidentally with the soliton at the coupling port [31]. This leads to a *local* increase in the resonant wavelength for this pump light. Thus there are effectively two resonant wavelengths, a smaller one determined by the round-trip phase shift including the Kerr shift from the CW background, and a larger one determined by the round-trip phase shift including the Kerr shift from the soliton [54]. The pump laser can be effectively blue-detuned with respect to the latter resonance, which can lead to thermally stable operation in the soliton regime.

Solitons are strongly localized: as can be seen from Eq. 1.26, the deviation of the background intensity from  $\rho_1$  near a soliton at  $\theta_0$  is proportional to  $e^{-(\theta-\theta_0)/\delta\theta}$ , where  $\delta\theta = \sqrt{-\beta_2/2\alpha}$ . If  $\delta\theta$  is sufficiently small, multiple solitons can be supported in the resonator domain  $-\pi \leq \theta \leq \pi$  with very weak interactions between solitons. If the separation between solitons  $i$  and  $j$  at  $\theta_i$  and  $\theta_j$  is small relative to  $\delta\theta$ , the solitons will interact. The topic of soliton interactions is complicated in general, with different types of interactions in different systems (see e.g. Refs. [55–58]). Simulations reveal that if  $(\theta_i - \theta_j)/\delta\theta$  is too small, LLE solitons exhibit attractive interactions as a result of the monotonic (as opposed to oscillatory) decay of the localized pulse to  $\psi_{CW}$  [59], which precludes the existence of stable equilibrium separations. The result of this attraction can be pair-wise annihilation or merger, with the ultimate result being an ensemble with fewer solitons. The maximum number of solitons that can coexist in a resonator in the absence of higher-order stabilizing effects (see Chapter ?? and Refs. [59, 60]) can be approximated as  $N_{max} \approx \sqrt{-2/\beta_2}$  [31]. An approximation to the form of a soliton ensemble is possible as:

$$\psi_{ens} = \psi_{CW,min} + e^{i\phi_0} \sqrt{2\alpha} \sum_j \operatorname{sech} \left( \sqrt{\frac{2\alpha}{-\beta_2}} (\theta - \theta_j) \right), \quad (1.27)$$

where  $\{\theta_j\}$  define the positions of the solitons in the ensemble and  $\phi_0 = \cos^{-1}(\sqrt{8\alpha}/\pi F)$  as above. Fig. 1.8 provides an example illustrating the degeneracy in soliton number of Kerr-combs operating in the soliton regime.

### 1.3.3.2 Microresonator solitons in experiments

Relative to the generation of extended modulation-instability patterns, experimental generation of solitons in microring resonators is challenging. Solitons are localized excitations below threshold, which means that their existence is degenerate with their absence—a resonator can host  $N = 0, 1, 2, \dots$  up to  $N_{max}$  solitons for a given set of parameters  $\alpha$  and  $F^2$ ; as discussed above and illustrated in Fig. 1.8. If  $\alpha$  and  $F^2$  are experimentally tuned to a point at which solitons may exist,  $\psi$  will evolve to a form determined by the initial conditions of the field  $\psi_0$ . To provide initial conditions that evolve to  $N > 0$  solitons, most experimental demonstrations of soliton generation

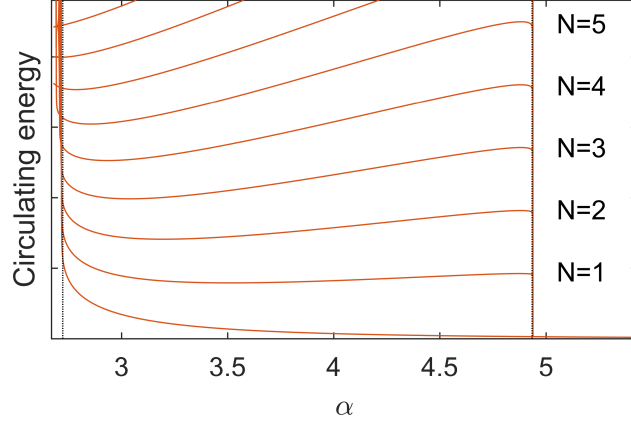


Figure 1.8: **Kerr-soliton energy-level diagram.** Some of the possible values of the circulating energy (proportional to  $\int d\theta |\psi|^2$ ) in the soliton regime as a function of the detuning parameter  $\alpha$ . Level curves correspond to the number of circulating solitons. This diagram is obtained from numerical solutions using  $F^2 = 4$ ,  $\beta_2 = -0.0187$ , and is quantitatively dependent on both of these parameters. Dotted vertical lines indicate approximations to the minimum and maximum detunings for solitons. The approximation for the minimum detuning is the value of  $\alpha$  at which the effectively red-detuned branch vanishes, obtained by inserting  $\rho_-$  (Eq. 1.18) into Eq. 1.16 for  $F^2 = 4$  and solving for  $\alpha$ , and the approximate maximum detuning is  $\alpha_{max} = \pi^2 F^2 / 8$ .

have involved first generating an extended pattern in the resonator, and then tuning to an appropriate point  $(\alpha, F^2)$  so that ‘condensation’ of solitons from the extended pattern occurs.

Condensation of solitons from an extended pattern presents additional challenges. First, it is difficult to control the number of solitons that emerge, due to the high degree of soliton-number degeneracy as shown in Fig. 1.8. This typically leads to a success rate somewhat lower than 100 % in the generation of single solitons. Second, the transition from a high duty-cycle extended pattern to a lower duty-cycle ensemble of one or several solitons comes with a dramatic drop in intracavity power that occurs on the timescale of the photon lifetime. If the resonator is in thermal steady-state before this drop occurs, the resonator will cool and the resonance frequency will increase. If this increase is large enough that the final detuning  $\alpha$  exceeds  $\alpha_{max} = \pi^2 F^2 / 8$ , the soliton is lost. This challenge can be addressed by preparing initial conditions for soliton generation and then tuning to an appropriate point  $(\alpha, F^2)$  faster than the cavity can come into thermal steady-state at the temperature determined by the larger power of the extended pattern; this is possible because the timescale over which an extended pattern can be generated is related to the photon lifetime, which

is typically much faster than the thermal timescale.

The first report of soliton generation in microresonators came in 2012 in a paper by Herr et al. [31] (2012 pre-print [30]). These authors described optimizing the speed of a decreasing-frequency scan of the pump laser across the cavity resonance so that solitons could be condensed from an extended pattern and the scan could then be halted at a laser frequency where the solitons could be maintained with the system in thermal steady-state at the temperature determined by the circulating power of the solitons. Stochastic reduction in the number of solitons in the resonator after condensation from an extended pattern was identified in these experiments. This corresponds to transitions between levels in the diagram in Fig. 1.8, and is associated with discrete steps in a measurement of the ‘comb power,’ the output power of the resonator with the pump frequency  $\nu_p$  filtered out. The resulting staircase-like nature of a comb power measurement is a useful experimental signature of soliton generation in microresonators, and is important for comparison with the results described in Chapter ??.

Other approaches for dealing with the challenges described above have been developed since this first demonstration; these include fast manipulation of the pump power [7, 61] or frequency [62], periodic modulation of the pump laser’s phase or power at  $f_{FSR}$  [14, 63], tuning of the cavity resonance frequency using chip-integrated heaters instead of tuning the pump-laser frequency [64, 65], and soliton-ensemble preparation and subsequent population reduction through manipulation of the pump laser [54]. These methods continue to make use of extended patterns to provide initial conditions for soliton generation. In formally-equivalent fiber-ring resonators, direct generation of solitons without condensation from an extended pattern has been demonstrated using transient phase and/or amplitude modulation of the pump laser [66–68].

### 1.3.3.3 Microresonator solitons in applications

Because solitons have single-FSR spacing, have the output localized into a high peak-power pulse, and are stationary (in contrast with chaos, which has single-FSR spacing but is not stationary), they are promising for applications. Many of the proposals for and demonstrations of applications

with Kerr-combs have used single-soliton operation. Some of the applications already demonstrated include an optical clock [69], dual-comb spectroscopy [70], coherent communications [71], and direct on-chip optical frequency synthesis [72]. Additionally, soliton combs have been self-referenced both with [73, 74] and without [75, 76] external spectral broadening. Nevertheless, there remains work to be done to bring microresonator-soliton technology to the level of maturity that will be required for deployment in the field. Chapters ?? and ?? describe two recent advancements: the development of a method for direct on-demand generation of single solitons by use of a phase-modulated pump laser, and the observation and explanation of a soliton-interaction mechanism that imparts rigid structure on the allowed configurations of multi-soliton ensembles.



## Chapter 2

### Downsampling of optical pulse trains

This chapter presents a discussion of a technique for repetition-rate reduction of optical pulse trains. While high pulse train repetition rates are appealing for some applications, they are not always appropriate. For example, spectral resolution in spectroscopy applications is sacrificed in a comb with a large mode spacing, and a high repetition rate makes nonlinear optics less efficient at a given average power. This can present a barrier to the generation of octave-spanning spectra for  $f - 2f$  self-referencing. On the other hand, in general the size of the comb package sets the scale for the round-trip time, meaning that low-SWAP combs tend to have inherently high repetition rates. Therefore, to increase the flexibility of low-SWAP and high-repetition-rate comb systems in applications, a method for reducing the repetition rate of a pulse train will be useful.

Here I present an investigation of a method for pulse train repetition-rate reduction, or down-sampling, in which an electro-optic gate realized by an RF-driven intensity modulator periodically transmits an incoming pulse at a frequency lower than the input repetition rate. The basic principle is illustrated in Fig. 2.1. Downsampling via pulse gating, also referred to as 'pulse picking' in the literature, has been used extensively in the context of high-field, phase-sensitive ultrafast optics for the generation of energetic, carrier-envelope-phase-stabilized ultrashort pulses [77, 78]. In this application, a comb with initial repetition rate in the  $\sim 100$  MHz range that has already been self-referenced and stabilized is pulse-picked to a repetition rate on the order of 1-100 kHz. Concerns in this application center around control and preservation of the carrier-envelope phase in the pulse-picking and amplification process [79, 80]. In contrast, the focus here is on downsampling within

the context of optical metrology with frequency combs, and we are concerned with downsampling's effect on the optical phase noise, the pulse-to-pulse energy fluctuations, and the carrier-envelope offset frequency of the comb. In particular, it is important that the downsampled pulse train is suitable for  $f - 2f$  self-referencing.

Sec. 2.1 presents a proof-of-principle experiment in which a 250 MHz pulse train is downsampled to 25 MHz, and then spectrally broadened and self-referenced. A mathematical model of downsampling is presented in Sec. 2.2, and this model informs the discussion of downsampling's effect on the pulse train's noise properties presented in Sec. 2.3 and Sec. 2.4. In Sec. 2.5 I discuss some practical considerations in applications of the technique, including the effect of imperfections in the gating process such as incomplete extinction of rejected pulses.

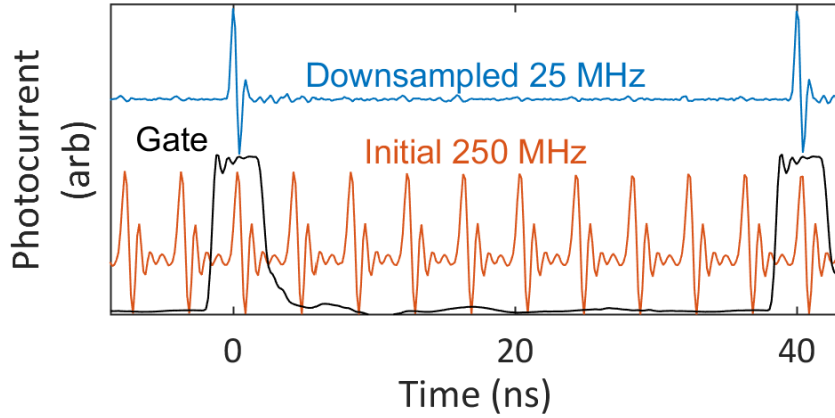


Figure 2.1: **An illustration of pulse-train repetition-rate downsampling.** Orange: A photodetected 250 MHz pulse train. Blue: A photodetected 25 MHz pulse train obtained by downsampling the 250 MHz pulse train by a factor of  $N = 10$ . Black: Oscilloscope trace showing the voltage sent to the RF port of a Mach-Zehnder intensity modulator to selectively transmit a subset of the incoming pulses. With the intensity modulator biased for zero transmission, the voltage trace is indicative of the transmission.

## 2.1 Proof-of-Concept Experiment

Here I present a proof-of-concept experiment in which a 250 MHz comb is downsampled and self-referenced. The setup for and results of this experiment are summarized in Fig. 2.2. Our pulse gating scheme, shown in Fig. 2.2a, employs a Mach-Zehnder (MZ) electro-optic intensity modulator

driven by 25 MHz rectangular electronic gating pulses with 80 ps transitions and 3.5 ns duration. The electronic pulse generator and the repetition rate of the input 250 MHz comb are both referenced to a hydrogen maser to maintain synchronization. The DC bias of the intensity modulator is set for maximum extinction outside the electronic gate, whose amplitude is approximately matched to  $V_\pi$  of the EOM. This downsampling scheme results in a stable 25 MHz optical pulse train with >12 dB contrast (Fig. 2.1). This contrast is adequate for this experiment, but could be improved by cascading modulators with higher extinction ratios. The average power of the 250 MHz pulse train is reduced from 30 mW to 400  $\mu$ W by the pulse gating process and the insertion loss of the optical components. The pulse train is amplified to 35 mW by use of a normal-dispersion erbium-doped fiber amplifier, which provides some spectral broadening and temporal pulse compression [81]. An octave-spanning supercontinuum is obtained by launching the amplified, <100 fs,  $\sim$ 1 nJ pulses into 20 cm of highly nonlinear fiber (HNLF) [82]; the resulting spectrum is shown in Fig. 2.2b. For comparison, we also present the supercontinuum generated by the 250 MHz comb with the EOM set for constant maximum transmission under otherwise identical conditions. The 250 MHz comb is amplified by the same EDFA to an average power of 85 mW, corresponding to 340 pJ pulse energy, before it enters the HNLF.

To detect  $f_0$ , the octave-spanning supercontinuum shown in Fig. 2.2b is sent into a free-space  $f - 2f$  interferometer consisting of a half-wave plate and a periodically poled lithium niobate (PPLN) crystal quasi-phase-matched for second-harmonic generation at 1980 nm. The generated 990 nm light is shown in 2.2b. A 10 nm band-pass filter at 990 nm selects this second harmonic and the co-linear supercontinuum at 990 nm, which are then photodetected to observe  $f_0$  with 30 dB signal-to-noise ratio, shown in Fig. 2.2c. Fig. 2.2d shows a 2000 s record of  $f_0$  for the downsampled comb.

## 2.2 Mathematical model for downsampling

While Fig. 2.2 presents an absolute frequency measurement of  $f_0$  enabled by downsampling, it does not demonstrate the deterministic connection between the input and downsampled combs

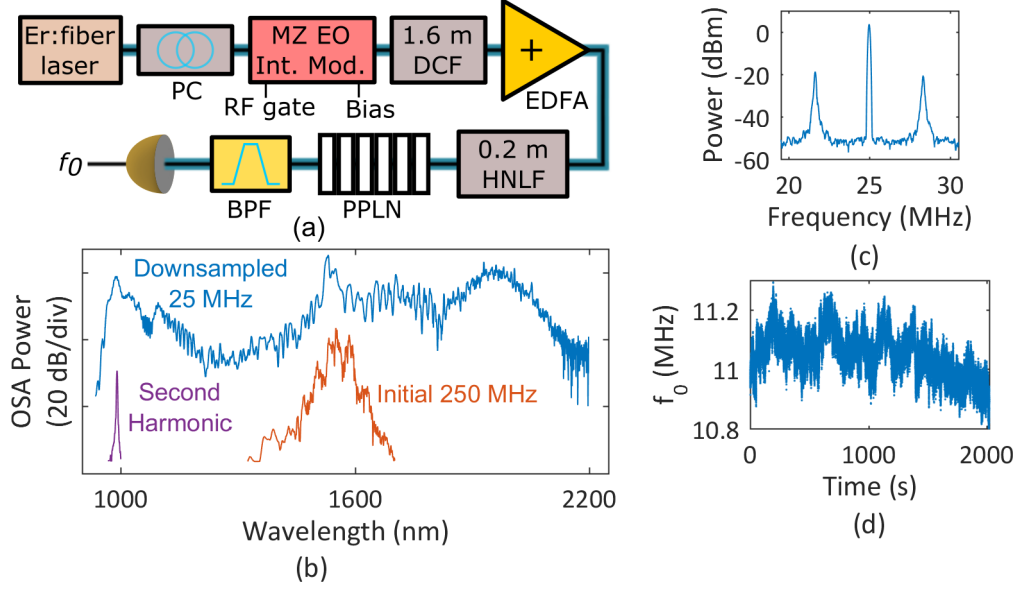


Figure 2.2: **Demonstration of downsampling for  $f_0$  detection.** (a) Schematic depiction of the setup for downsampling a 250 MHz Er:fiber comb and detecting the offset frequency of the resulting 25 MHz pulse train. PC—polarization controller. DCF—dispersion-compensating fiber. EDFA—erbium-doped fiber amplifier. HNLF—highly nonlinear fiber. PPLN—periodically-poled lithium niobate. BPF—(optical) band-pass filter. (b) Octave-spanning supercontinuum generated by downsampling (top, blue), second harmonic generated for  $f_0$  detection (purple), and for comparison the supercontinuum generated by the same apparatus without downsampling (orange). (c) Detected repetition rate and  $f_0$  beat at 100 kHz resolution bandwidth; signal-to-noise ratio of  $f_0$  is 30 dB. (d) Counted frequency of the detected free-running offset beat. Data is taken for  $\sim 2000$  s at 10 ms gate time. The offset frequency of the 250 MHz commercial comb was adjusted between measurements shown in Figs. 2.2c and 2.2d to simplify electronic processing.

that is essential for applications. To understand this relationship, I present first a simple model of downsampling, and then experimental tests of its conclusions.

The downsampled pulse train's electric field is modeled as the product of the incoming comb's field and a time-varying amplitude modulation. For an incoming optical frequency comb with repetition rate  $f_{rep}$ , complex single-pulse field  $A(t)$  that is localized near  $t = 0$ , and pulse-to-pulse carrier-envelope phase shift  $\phi$ , pulse gating by a train of rectangular pulses of length  $t_g$  and arrival rate  $f_g$  yields a downsampled comb with field

$$a(t) = [\sum_n A(t - n/f_{rep})e^{in\phi}] \times [\sum_m \text{Rect}((t - m/f_g)/t_g)] \quad (2.1)$$

where  $\text{Rect}(x)$  is the rectangle function, taking the value 1 for  $-1/2 \leq x \leq 1/2$  and 0 elsewhere. Indices  $n$  and  $m$  count the pulse number of the incoming pulse train and the electronic gate respec-

tively. The optical spectrum of the downsampled pulse train  $a(t)$ , calculated via the convolution theorem for the Fourier transform, is:

$$\mathcal{F}\{a\}(f) \sim 4\pi f_{rep} \sum_{nm} \frac{1}{m} \mathcal{F}\{A\}(f_0 + n f_{rep}) \times \sin(\pi m t_g f_g) \delta(f - f_0 - n f_{rep} - m f_g) \quad (2.2)$$

where  $f_0 = f_{rep} \cdot \phi / 2\pi$  is the carrier-envelope offset frequency of the incoming comb and  $\delta$  is the Dirac delta function. The downsampled pulse train has spectral content at optical modes  $f_0 + n f_{rep}$ , as well as at intensity modulation sidebands whose frequency offsets  $m f_g$  are harmonics of the gating frequency. To avoid the generation of unwanted modulations, pulse gating at an integer sub-harmonic of the incoming repetition rate,  $f_g = f_{rep}/N$ , is essential. In this case superposition of the intensity modulation components created by pulse gating results in a downsampled frequency comb with a single mode spacing. Moreover, this model predicts that the offset frequency is preserved up to a reduction modulo the comb's new repetition rate.

Notably, for pulse gating at a sub-harmonic of the input comb's repetition rate, timing jitter of the electronic gate that is less than its duration does not contribute to noise on the downsampled comb. By modeling jitter as gate-to-gate arrival-time delays  $\Delta t_m$ , it can be shown that the downsampled comb's amplitude  $a(t)$  and spectrum  $\mathcal{F}\{a\}(f)$  do not deviate from Eqn. 2.1 provided that: (1) The jitter is a sufficiently small  $|\Delta t_m| < t_g/2$ , i.e., that the optical and electronic pulses are always substantially overlapped, and (2) That the optical pulses are substantially shorter than the electrical pulses, which is true for most systems. Thus, in general we expect that the carrier-envelope offset frequency of the incoming comb is preserved by downsampling even with jitter on the gate signal.

### 2.3 Experimental investigation of the effect of downsampling on the pulse train's noise properties

We supplement the mathematical model presented above with an experimental investigation of the effects of downsampling on the noise properties of the pulse train. First we consider the effects of technical limitations to ideal downsampling, and then we discuss fundamental effects associated

with aliasing of high-Fourier-frequency optical noise and shot noise.

We measure the phase-noise spectrum of the downsampled comb's repetition rate at different points in our apparatus, as shown in Fig. 2.3a. We also plot the phase noise of the 250 MHz comb, which has been shifted by  $-10\log_{10}(N^2) = -20$  dB to facilitate comparison [83], and the phase noise of the electronic gate. The downsampled frequency comb's phase-noise spectrum matches that of the 250 MHz comb except for a small increase at  $\sim 3$  kHz, likely corresponding to the corner in the gate generator's phase noise at the same frequency. The phase noise of the high- and low-frequency ends of the supercontinuum similarly matches the 250 MHz comb below 1 kHz. The higher phase noise in the supercontinuum beyond 1 kHz is above the measurement system's noise floor (including shot noise), despite the reduced optical power available after spectral filtering. This higher noise is likely due to noise generation processes in the HNLF, such as the conversion of amplitude fluctuations on input pulses to timing jitter in the supercontinuum [84].

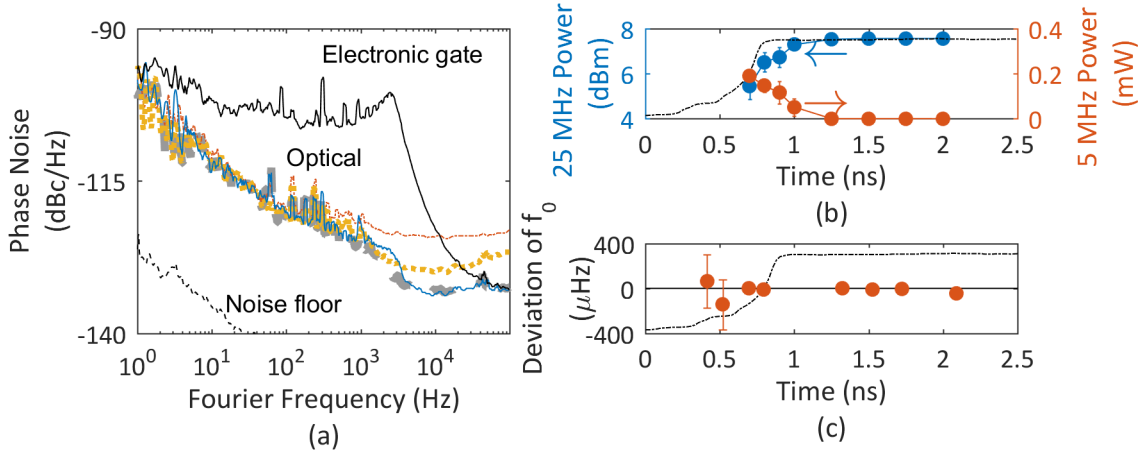


**Figure 2.3: Experimental investigation of noise introduced by downsampling.** (a) Measured repetition-rate phase noise of spectral components of the supercontinuum, selected by a  $990 \pm 5$  nm band-pass filter (dot-dashed orange), 1650 nm long pass filter (dotted yellow), and the entire downsampled 25 MHz frequency comb measured immediately before the EDFA (solid blue), the 250 MHz comb (large-dashed gray, shifted by  $20 \log(1/10) = -20$  dB). Also shown is the phase noise of the electronic gate generator (top, solid black). (b) Amplitude of the downsampled pulse-train modulation due to 250 ps jitter at 5 MHz rate. The position of a data point on the x-axis indicates its mean position within the gate, shown in dashed black. Measurement uncertainties arise due to a latency between the optical trigger and the start of the electronic gating signal which varies on the order of 50 ps. (c) Deviation of the carrier-envelope offset frequency of the downsampled comb from the 250 MHz comb's offset frequency as a function of the alignment of optical pulses within the gate.

The timing jitter of our gating pulse train is between 5 ps (obtained by integrating the phase noise plotted in Fig. 2.3 to 100 kHz) and 10 ps (extrapolating constant phase noise to the 12.5 MHz Nyquist frequency and integrating). These jitter values are small relative to the 4 ns repetition period of the incoming optical pulse train. As the repetition rate of the incoming optical pulse train increases to  $>10$  GHz, the gate duration must correspondingly decrease for single-pulse gating, and timing jitter on the gate may become a significant fraction of the gate duration. To explore the effects of timing jitter larger than our pulse generator's inherent 5 to 10 ps, we impose excess jitter on the gating signal. We modulate the relative timing between the gating signal and the incoming optical pulse train at a frequency of 5 MHz with an amplitude of 250 ps. The effect of this jitter is manifest in the microwave power of the gated comb as 5 MHz intensity-modulation sidebands whose amplitude depends on the position of the optical pulses within the gate, as shown in Fig. 2.3b. Pulses with a mean position within 250 ps of the gate edge are substantially modulated by the 5 MHz gate-delay signal. This agrees with the prediction of a sharp threshold on the acceptable level of timing jitter on the gate.

It is essential to establish that the comb's carrier-envelope offset frequency is preserved in the downsampling process. To do this, we perform a frequency comparison of the 25 MHz downsampled comb and a separate output of the 250 MHz comb. This 250 MHz output is intensity modulated so that a measurement of the nonzero optical heterodyne beat frequency between an intensity modulation sideband and a pulse-gating sideband of the downsampled comb reveals the relative frequency offset of the two combs. Figure 2.3c shows the null frequency shift between the 25 MHz and 250 MHz combs, which we have characterized for different alignments of the optical pulse within the gate. At the level of several microhertz, better than  $10^{-18}$  relative to the 200 THz optical carrier frequency, we observe no frequency shift between the 250 MHz comb and the downsampled 25 MHz comb when the gate is properly aligned. This confirms the utility of downsampling for measurement of a high-repetition-rate comb's offset frequency for subsequent use of the comb in, for example, a spectroscopy experiment requiring high power per comb mode and high frequency precision.

## 2.4 Effects of ideal downsampling on a pulse train's noise properties

In addition to the conversion of electronic technical noise to optical noise on the downsampled pulse train, there exists a further mechanism by which downsampling can change the measured amplitude noise properties of the pulse train. Even ideal downsampling, free of electronic noise, leads to an increase in the measured power spectral density (PSD) of optical pulse energy fluctuations (PEF) when technical pulse energy noise is present. This is due to aliasing of components of the PSD of pulse energy fluctuations at frequencies above the Nyquist frequency of the original pulse train,  $f_{rep}/2$ , when the Nyquist frequency is reduced to  $f_{rep}/2N$  by downsampling. Assuming random fluctuations from pulse to pulse, downsampling does not change the RMS fractional pulse energy fluctuation  $\sigma_{PEF}$ , whose square is equal to the frequency integral of the PSD of pulse energy fluctuations  $S_{PEF}(f)$ :

$$\sigma_{PEF}^2 = \int_0^{f_{rep}/2} df S_{PEF}(f). \quad (2.3)$$

—

Because the Nyquist frequency defines the upper limit for integration of  $S_{PEF}$ , in order for  $\sigma_{PEF}$  to be preserved  $S_{PEF}(f)$  must increase when the Nyquist frequency is reduced by downsampling. For example, in the simple case of white technical noise on the pulse energies with density  $S_o$ , we have

$$\sigma_{PEF}^2 = \int_0^{f_{rep}/2} df S_o = \int_0^{f_{rep}/2N} df S' \quad (2.4)$$

which shows that downsampling must increase the measured PSD of white technical noise from  $S_o$  to  $S' = NS_o$ , assuming there are no spectral correlations. However, this simple multiplicative increase is restricted to the case of white technical noise. In general, the PSD of pulse energy fluctuations of the new pulse train is determined from the original PSD through the usual method of modeling aliasing of a signal: a new Fourier frequency for each component of the original PSD is obtained by reducing the original Fourier frequency by a multiple of  $-f_{rep}/N$  so that it lies between  $-f_{rep}/2N$  and  $f_{rep}/2N$  and taking its absolute value. The new PSD is then determined



by taking the quadrature sum of the PSD components at the same aliased Fourier frequency. This phenomenon is derived mathematically and demonstrated experimentally in Ref. [79], where the analysis of carrier-envelope phase noise applies equally well to pulse energy fluctuations.

In contrast with the increase in the PSD of pulse energy fluctuations arising from coincidence of the optical pulse with the edge of the electrical gate, which increases  $\sigma_{PEF}$ , the aliasing mechanism described above preserves  $\sigma_{PEF}$ . An important consequence of this is that while technical noise can lead to supercontinuum decoherence in external nonlinear spectral broadening, aliasing does not, because it is  $\sigma_{PEF}$  which determines the degree of supercontinuum decoherence. Thus the aliasing mechanism impedes  $f - 2f$  self-referencing only by reducing the available signal-to-noise ratio of an  $f_0$  signal in a straightforward linear fashion.

In practice, the relevance of the aliasing of the PSD of pulse energy fluctuations is determined by the presence of technical noise on the pulse energies at high Fourier frequency  $f > f_{rep}/2N$ . For sufficiently small downsampling factors (e.g.  $f_{rep}/2N \leq \sim 50MHz$ ) and depending on the comb source, it is possible that the only source of intensity noise at frequencies above  $f_{rep}/2N$  is shot noise. Shot noise results in a maximal (shot-noise-limited) signal-to-noise ratio (SNR) of an optical heterodyne beat with a local oscillator laser which is reduced by  $N^2$  (in electrical power units) as the average power of the pulse train is reduced by downsampling by a factor of  $N$ . In contrast, in the case of detection of a carrier-envelope-offset beat with fixed optical detection bandwidth, the shot-noise-limited SNR is preserved in downsampling. One way to understand these results is to model the shot noise at a given Fourier frequency as the incoherent sum of optical heterodyne beats between each optical comb mode and the uncorrelated vacuum fluctuations at the appropriate optical frequency [85, 86], and to take into account the fact that during downsampling the optical power of each comb mode is reduced by  $N^2$ , with the first factor of  $N$  coming from reduction of the total optical power and the second factor of  $N$  due to the increase in the spectral density of comb modes.

We experimentally investigate the impact of downsampling on the PSD of pulse energy fluctuations by measuring noise on three photodetected optical signals: a shot-noise-limited telecom-band

CW laser, a 10 GHz pulse train generated by passing this laser through cascaded optical phase and intensity modulators (see Chapter ??, [87]) and then a low-noise EDFA, and this pulse train after downsampling by a factor of four to 2.5 GHz repetition rate with no additional amplification after downsampling. Shown in Figure 2.4 are curves for each signal of the fluctuations  $\sqrt{S_I(f = 50 \text{ MHz})}$  in the detected photocurrent at a Fourier frequency of 50 MHz versus the total time-averaged detected photocurrent  $\langle I \rangle$  from the optical signal. To measure the scaling of noise with optical power, these curves are generated by beginning with an optical signal which yields more than 800  $\mu\text{A}$  of detected photocurrent and attenuating this signal before photodetection. The data indicate that both the pulse-generation process and the downsampling process contribute some amount of technical noise at 50 MHz Fourier frequency to the photocurrent, because the measured curves are well-modeled by a quadrature sum of a shot-noise contribution and a technical noise contribution. The contributions of these two types of noise can be determined because they scale differently with the photodetected power: shot noise obeys the relationship  $\sqrt{S_I(f = 50 \text{ MHz})} = \sqrt{2e \langle I \rangle}$ ,  $\langle I \rangle$  denoting the time-averaged photocurrent, while the technical-noise contribution arises from fluctuations in the expected photocurrent  $I(t)$  and scales linearly with the detected photocurrent. We observe that downsampling by a factor of four leads to a multiplication of the amplitude of the technical noise by a factor of  $\sim 1.7$  on the optical signal relative to the carrier, which due to finite noise bandwidth is somewhat less than the factor of two (four, in electrical power units) that would be expected for ideal downsampling by a factor of four in the presence of white technical noise. These results further demonstrate that, properly implemented, downsampling does not magnify noise on the pulse train to a degree that is prohibitive for applications.

## 2.5 Model for the effect of incomplete extinction of rejected pulses and amplification of a downsampled pulse train

To this point, we have considered effects of downsampling assuming that extinction of the rejected pulses is complete, but in a practical application this is not necessarily the case. The modulators used for pulse extinction may transmit a substantial amount of energy from the rejected

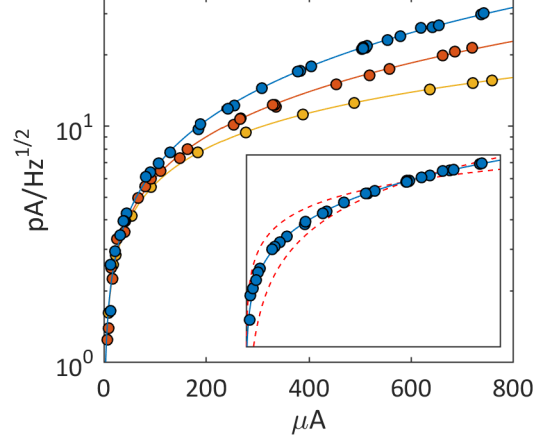


Figure 2.4: **Effect of downsampling on photocurrent fluctuations.** Fluctuations at 50 MHz Fourier frequency in the detected photocurrent as a function of the time-averaged photocurrent in three cases: CW laser at the shot-noise limit (lowest, yellow), 10 GHz pulse train (middle, red), and 2.5 GHz downsampled pulse train (highest, blue). Dots show measured data and curves show fits to the data. The fit for the shot-noise-limited laser has a single free parameter, which is a scaling factor of order 1 due to frequency dependence of the photodetector’s transimpedance gain. The fits for the pulse trains have a scaling factor in common, and have as an additional parameter the amplitude of the technical noise on the pulse train. This is -153.9 dBc/Hz for the 10 GHz pulse train and increases by a factor of  $\sim 1.72$  to -149.3 dBc/Hz for the 2.5 GHz downsampled pulse train. Inset: Optimized fits (dashed red) to the experimental data for the downsampled 2.5 GHz pulse train using only shot noise or linear technical noise scaling, demonstrating that both noise processes are important for explaining the data.

pulses—for example, one commercial manufacturer specifies 25 dB extinction ratio, and this number vary in practice. Additionally, the electronic gating signal may not have sufficient bandwidth to completely switch from transmission to extinction within the repetition period of the incoming pulse train, and initial extinction can be followed by some transmission caused by ringing in the gating signal. Bandwidth limitations will be increasingly likely as the repetition rates of frequency combs increase, placing more demanding requirements on gating electronics. Incomplete extinction will add modulations to the optical spectrum and will raise the total power of the downsampled pulse train while keeping the energy of the fully-transmitted pulses fixed. This will require higher average power to achieve a given target pulse energy.

The effects of incomplete extinction of rejected pulses are exacerbated if the incomplete extinction does not happen in a deterministic and repetitive fashion; this could occur, for example, if intermediate pulses fall near the edge of the gate in the presence of relative timing jitter between

the optical and electronic pulse trains, or if the extinction ratio fluctuates in time. Interestingly, if the downsampled pulse train is subsequently amplified and spectrally broadened, the impact of incomplete extinction depends on whether the optical amplifier used operates in the linear regime or in the saturated regime.

As an example, we consider the case where each fully transmitted pulse is preceded and followed by partially-extinguished pulses whose amplitudes fluctuate for each period of the downsampled pulse train. This fluctuation could occur because the pulses lie on the edge of the electronic gate and there is relative timing jitter between the optical pulse train and the gating signal. It is true that these fluctuations will lead to decoherence during nonlinear spectral broadening. However, the coherence is degraded by this mechanism only within the bandwidth that is achieved by the broadened, partially-extinguished pulses. In efficient  $f - 2f$  interferometry only the fully-transmitted pulses should reach an octave in bandwidth. Therefore, this mechanism of supercontinuum decoherence is not a problem in  $f - 2f$  interferometry in general, unless there is coupling between the amplitudes of the amplified partially-extinguished pulses and the amplified fully-transmitted pulses. This coupling can arise, for example, through amplification in the saturation regime, which then leads to decoherence across the full bandwidth of the supercontinuum.

To illustrate this point, we have performed numerical simulations of the spectral broadening of a 100 GHz train of 100 fs pulses which has been downsampled to 10 GHz and then amplified. We use an adaptive [88] split-step Fourier method [89] to simulate spectral broadening in 30 cm of HNLF according to the generalized nonlinear Schrodinger equation [17] (see Appendix A). In the simulation each fully-transmitted pulse, amplified to 1 nJ, is preceded and followed by partially-extinguished pulses with normally distributed and uncorrelated energies with mean of 0.3 nJ and standard deviation of 0.225 nJ. This models the effect of adjacent pulses that coincide with the edge of the gate. We simulate amplification in two regimes: saturation is simulated using a fixed-energy method wherein the pulse energies in each three-pulse burst are rescaled by a common factor so that the total energy is 1.6 nJ; linear amplification is simulated using a fixed-gain model, which involves no such rescaling of pulses. Numerically, we simulate the spectral broadening of each pulse

individually, which is acceptable because terms in the generalized nonlinear Schrodinger equation operate only locally or, in the case of the Raman term, on the timescale of several femtoseconds, while the separation between the pulses in each burst is 10 ps (the inverse of the initial 100 GHz repetition rate). We have verified that during simulated time-evolution each broadened pulse remains well-centered in its 5 ps simulation window.

Results of this study are shown in Figure 2.5. Figure 2.5a depicts a three-pulse burst before and after propagation in HNLF. In Figure 2.5b we show spectra corresponding to spectral broadening of this three-pulse burst, as well as plots of the spectral coherence averaged over many simulations. The first-order spectral coherence  $g_{12}^{(1)}(\lambda)$  is defined as:

$$\left| g_{12}^{(1)}(\lambda) \right| = \left| \frac{\langle E_1^*(\lambda) E_2(\lambda) \rangle}{\sqrt{\langle |E_1(\lambda)|^2 \rangle \langle |E_2(\lambda)|^2 \rangle}} \right| = \left| \frac{\langle E_1^*(\lambda) E_2(\lambda) \rangle}{\langle |E(\lambda)|^2 \rangle} \right|. \quad (2.5)$$

Curves are plotted for the fixed-gain and fixed-energy cases, as well as for the case with ideal downsampling (no partially-extinguished pulses) and only shot-noise on the pulse train. The averages in the formula above are over 1000 instantiations of the pair  $E_1$  and  $E_2$ , for a total of 2000 broadened spectra for each pulse within the burst of three. In both the fixed-gain and fixed-energy cases the coherence is poor in the center of the spectrum, but in the fixed-gain case, which models amplification in the linear regime, the coherence is preserved in the high- and low-frequency ends of the spectrum where it is needed for self-referencing.

## 2.6 Further remarks on the application of downsampling

Downsampling via pulse gating is a promising tool to manipulate high-repetition-rate frequency combs from low size, weight, and power packages and to aid in the detection of their offset frequencies. In our experiments downsampling enabled detection of  $f_0$  at a signal-to-noise ratio sufficient for measurement and stabilization, which otherwise would have required significantly higher average power. The effects of the electronic timing jitter of the gate signal are negligible so long as incoming optical pulses do not arrive coincidentally with the edge of the gate; when they do, timing jitter induces amplitude noise on the transmitted pulses. This results in an increase in RMS optical pulse

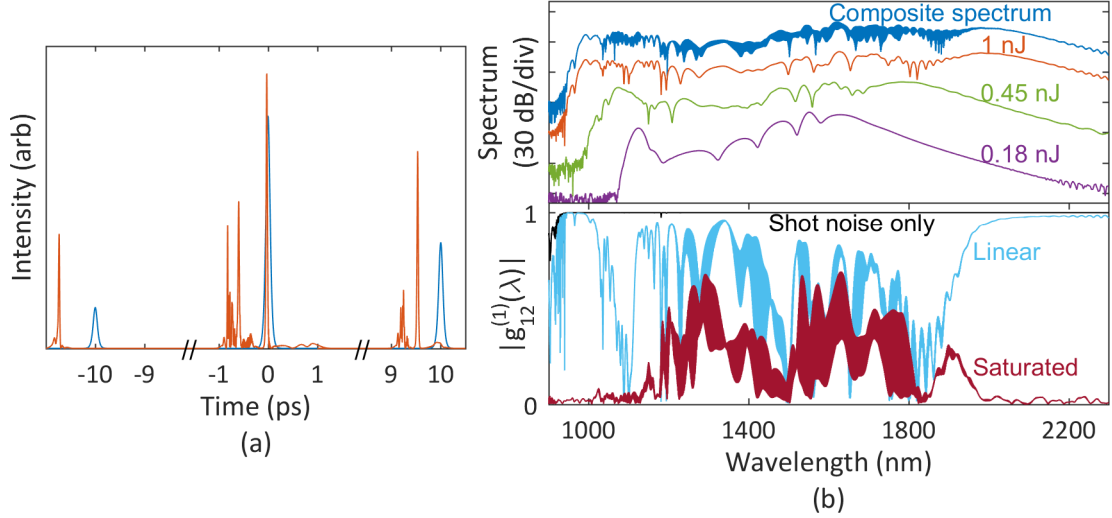


Figure 2.5: **Investigation of incomplete pulse extinction and amplification.** (a) A burst consisting of a fully-transmitted 1 nJ, 100 fs pulse and 100 fs partially-transmitted adjacent pulses with energies of 0.18 nJ and 0.45 nJ. Blue indicates initial  $\text{sech}^2$  pulses, and orange indicates the intensity after propagation through 30 cm HNLF. Note that the  $x$ -axis has been broken. (b) Top panel: optical spectra corresponding to the pulses shown in orange in (a), showing the composite spectrum of the three pulses (top, blue) and the spectra of the 1 nJ central pulse (second, orange), the 0.45 nJ adjacent pulse (third, green), and the 0.18 nJ adjacent pulse (bottom, purple). Bottom panel: Calculated spectral coherence averaged over 2000 simulations for the case of shot noise only (top, black) and for the case of fluctuating amplitudes of the first and third pulses as described in the text, after simulated amplification in a linear-regime optical amplifier (second, teal), and a saturated optical amplifier (bottom, maroon). For the case of linear-regime operation, high spectral coherence is preserved in the extreme ends of the supercontinuum even as it is lost in the center, in contrast with the complete loss of coherence after amplification in saturation.

energy fluctuations  $\sigma_{PEF}$ . Independently, the PSD of pulse energy fluctuations may be increased by aliasing of technical noise and by shot noise, depending on the relative magnitudes of these two types of noise. Each of these sources of signal-to-noise-ratio degradation has the potential to interfere with detection of  $f_0$ . This investigation of these challenges will facilitate application of the technique in high-repetition-rate frequency comb systems. Importantly, our experiments demonstrated that downsampling does not add a significant amount of noise to the frequency components of the pulse train, and in a separate experiment the technique has recently been used successfully to detect the carrier-envelope offset frequency of a 10 GHz comb by downsampling by a factor of four ([90], see Chapter ??).

To employ downsampling as demonstrated here with repetition rates  $>10$  GHz will require

electronic gates with duration  $\leq 100$  ps. Technology to downsample with gates as short as 20 ps is commercially available, while 100 Gb/s integrated circuits and 25 GHz demultiplexing have been demonstrated [91, 92]. Barring the use of such state-of-the-art electronics, pulse gates of duration longer than the incoming optical pulse train's repetition period can be employed. This will be technically easier to achieve, but will result in additional modulations on the spectrum of the downsampled pulse train.

The ambiguity of the input comb's offset frequency as a result of the reduction of the offset frequency modulo the new repetition rate makes downsampling most suitable for applications where the ambiguity can be removed by some other method. Two such applications are frequency comb calibration of astronomical spectrographs, where measurement of the wavelength of a comb mode can remove the ambiguity, and microresonator-based frequency combs, where the uncertainty in the offset frequency is determined by the frequency stability of the pump laser and can be much less than the repetition rate of the downsampled comb.

## Appendix A

### Numerical simulations of nonlinear optics

This appendix describes the algorithm used for numerical simulation of the generalized nonlinear Schrodinger equation (GNLSE) and Lugiato-Lefever equation (LLE) to obtain the results presented in the preceding chapters in this thesis. These equations are simulated with Matlab using a fourth-order Runge-Kutta interaction picture (RK4IP) method [89] with adaptive step size [88]. The RK4IP method is a particular algorithm in the broader class of split-step Fourier algorithms, in which nonlinearity is implemented in the time domain and dispersion is implemented in the frequency domain. An illustrative example of this split-step Fourier approach is a far simpler algorithm carried out with a single line of Matlab code to simulate the LLE:

```
psi=ifft(exp(delta*L).*fft(exp(delta*(1i*abs(psi).^2+F./psi)).*psi));
```

where  $\delta$  is the step size and  $L$  is a linear frequency-domain dispersion operator ( $\hat{L}$ , see below) that has been defined in the preceding code. The RK4IP algorithm with adaptive step size is advantageous over this simple algorithm in calculation time and in the scaling of error with the step size.

#### A.1 RK4IP algorithm

The LLE (NLSE) describes the evolution of the field  $\psi(A)$ , a function of a fast variable  $\theta(T)$ , over a timescale parametrized by a slow variable  $\tau(z)$ . In what immediately follows we use the variable names corresponding to the LLE for simplicity. Each of these equations can be written as the sum of a nonlinear operator  $\hat{N}$  and a linear operator  $\hat{L}$  acting on  $\psi$ , so that the field  $\psi$  evolves



as

$$\frac{\partial \psi}{\partial \tau} = (\hat{N} + \hat{L})\psi, \quad (\text{A.1})$$

which can be implemented with the split-step Fourier approach.

The RK4IP algorithm specifies a recipe for advancing the field a single step  $\delta$  in the slow variable  $\tau$  to obtain  $\psi(\theta, \tau + \delta)$  from  $\psi(\theta, \tau)$ . This specific algorithm has the attractive feature that it reduces the number of Fourier transformations that must be performed to achieve a given calculation accuracy relative to other common algorithms. The RK4IP algorithm is [89]:

$$\psi_I = \exp\left(\frac{\delta}{2}\hat{L}\right)\psi(\theta, \tau) \quad (\text{A.2})$$

$$k_1 = \exp\left(\frac{\delta}{2}\hat{L}\right)\left[\delta\tau\hat{N}(\psi(\theta, \tau))\right]\psi(\theta, \tau) \quad (\text{A.3})$$

$$k_2 = \delta\hat{N}(\psi_I + k_1/2)[\psi_I + k_1/2] \quad (\text{A.4})$$

$$k_3 = \delta\hat{N}(\psi_I + k_2/2)[\psi_I + k_2/2] \quad (\text{A.5})$$

$$k_4 = \delta\hat{N}\left(\exp\left(\frac{\delta}{2}\hat{L}\right)(\psi_I + k_3)\right) \quad (\text{A.6})$$

$$\times \exp\left(\frac{\delta}{2}\hat{L}\right)(\psi_I + k_3) \quad (\text{A.7})$$

$$\psi(\theta, \tau + \delta) = \exp\left(\frac{\delta}{2}\hat{L}\right)[\psi_I + k_1/6 + k_2/3 + k_3/3] + k_4/6. \quad (\text{A.8})$$

In the above it is understood that  $\hat{L}$  is applied in the frequency domain and  $\hat{N}$  is applied in the time domain. Calculation of  $\psi(\theta, \tau + \delta)$  from  $\psi(\theta, \tau)$  therefore requires eight Fourier transformations.

## A.2 Adaptive step-size algorithm

An adaptive step-size algorithm is a strategy for adjusting the magnitude of the steps  $\delta$  that are taken to optimize the simulation speed while maintaining a desired degree of accuracy. The RK4IP algorithm exhibits error that scales locally as  $O(\delta^5)$ . Since reducing the step size naturally requires more steps and therefore increases the number of small errors that accumulate, the resulting global accuracy of the algorithm is  $O(\delta^4)$ . One appropriate step-size adjustment algorithm for this scaling is described by Heidt [88]. For a given goal error  $e_G$ , the algorithm goes as follows:

- Calculate a field  $\psi_{coarse}$  by advancing the field  $\psi(\theta, \tau)$  according to RK4IP by a step of size  $\delta$ .
- Calculate a field  $\psi_{fine}$  by advancing the field  $\psi(\theta, \tau)$  according to RK4IP by two steps of size  $\delta/2$ .
- Calculate the measured error  $e = \sqrt{\sum_j |\psi_{coarse,j} - \psi_{fine,j}|^2 / \sum_j |\psi_{fine,j}|^2}$ , where  $j$  indexes over the discrete points parametrizing the fast variable  $\theta$ .
  - \* If  $e > 2e_G$ , discard the solution and repeat the process with coarse step size  $\delta' = \delta/2$ .
  - \* If  $e_G < e < 2e_G$ , the evolution continues and the step size is reduced to  $\delta' = \delta/2^{1/5} \approx 0.87\delta$ .
  - \* If  $e_G/2 < e < e_G$ , the evolution continues and the step size is not changed.
  - \* If  $e < e_G/2$ , the evolution continues and the step size is increased to  $\delta' = 2^{1/5}\delta \approx 1.15\delta$ .

When the simulation continues, the new field  $\psi(\theta, \tau + \delta)$  is taken to be  $\psi(\theta, \tau + \delta) = 16\psi_{fine}/15 - \psi_{coarse}/15$ . In the calculations described in this thesis, the goal error  $e_G$  is typically  $10^{-6}$ .

### A.3 Pseudocode for numerical simulation with the RK4IP algorithm and adaptive step size

The pseudocode shown in Algorithm 1 shows how the RK4IP algorithm with adaptive step size is implemented. This pseudocode neglects the specific details of the RK4IP algorithm.

Two notes:

- The current field  $\psi(\theta, \tau)$  is stored until the approximation to the new field  $\psi(\theta, \tau + \delta)$  is found to be acceptable.
- This implementation makes use of an extra efficiency that is possible when the solution is discarded and the step size is halved: the first step of the fine solution  $\psi_{fine,1}$  for the previous attempt becomes the coarse solution  $\psi_{coarse}$  for the current attempt.

---

**Algorithm 1** Pseudocode showing the implementation of RK4IP with adaptive step size.

---

```

procedure
  while  $\tau < \tau_{end}$  do
     $e = 1$  ▷ Initialize the error to a large value
     $firsttry = TRUE$  ▷ For more efficiency if this is not the first attempt (see below)
     $\delta = 2\delta$  ▷ To account for halving on the first iteration

    while  $e > 2e_G$  do
      if  $firsttry$  then
         $\psi_{coarse} = \text{RK4IP}(\psi, \delta)$ 
      else
         $\psi_{coarse} = \psi_{fine,1}$  ▷ We get to re-use the first step of the previous attempt's fine solution

       $\delta = \delta/2$ 
       $\psi_{fine} = \psi$ 

      for  $j_{step} = 1 : 2$  do
         $\psi_{fine} = \text{RK4IP}(\psi_{fine}, \delta)$ 
        if  $j_{step} = 1$  then
           $\psi_{fine,1} = \psi_{fine}$ 

       $e = \sqrt{\sum |\psi_{coarse} - \psi_{fine}|^2 / \sum |\psi_{fine}|^2}$ 
       $firsttry = FALSE$ 

       $\psi = 16\psi_{fine}/15 - \psi_{coarse}/15$ 
       $\tau = \tau + 2\delta$  ▷ We took two fine steps of size  $\delta$ 

      if  $e > e_G$  then
         $\delta = \delta/2^{1/5}$ 
      if  $e < e_G/2$  then
         $\delta = 2^{1/5}\delta$ 

```

---

### A.3.1 Simulation of the LLE

For simulation of the LLE, the operators are:

$$\hat{N} = i|\psi|^2 + F/\psi, \quad (\text{A.9})$$

$$\hat{L} = -(1 + i\alpha_\mu), \text{ where} \quad (\text{A.10})$$

$$\alpha_\mu = \alpha - \sum_{n=1}^N \beta_n \mu^n / n!. \quad (\text{A.11})$$

The subscript  $\mu$  indicates the pump-referenced mode number upon which the operator acts. Note, in particular, that the pump term  $F$  has been incorporated into the nonlinear operator, so that it is implemented in the time domain. The quantity  $\hat{N}\psi$  then becomes  $i|\psi|^2\psi + F$ , as required for computation of  $\partial\psi/\partial\tau$ .

### A.3.2 Simulation of the GNLSE

In addition to self-phase modulation, the GNLSE used in the simulations conducted for Chapter 2 contains nonlinear terms that describe the medium's Raman response and self-steepening. The equation employed can be written as [17, 89]:

$$\frac{\partial A}{\partial z} = - \left( \sum_n \beta_n \frac{i^{n-1}}{n!} \frac{\partial^n}{\partial T^n} \right) A + i\gamma \left( 1 + \frac{1}{\omega_0} \frac{\partial}{\partial T} \right) \times \left( (1 - f_R)A|A|^2 + f_RA \int_0^\infty h_R(\tau)|A(z, T - \tau)|^2 d\tau \right). \quad (\text{A.12})$$

For Chapter 2, second- and third-order dispersion is used with  $\beta_2 = -7.7 \text{ ps}^2/\text{km}$  and  $\beta_3 = 0.055 \text{ ps}^3/\text{km}$ , where  $\beta_n$  is the  $n^{\text{th}}$  frequency-derivative of the propagation constant. The nonlinear coefficient  $\gamma = \frac{2\pi}{\lambda} \frac{n_2}{A_{eff}}$  used is  $11 \text{ W/km}$  [82], coming from an effective mode-field diameter of  $\sim 3.5 \text{ }\mu\text{m}$  for the HNLF used in the experiment and the nonlinear index  $n_2 = 2.7 \times 10^{-16} \text{ cm}^2/\text{W}$  of silica. The quantity  $\omega_0 = 2\pi c/\lambda_0$  is the (angular) carrier frequency of the pulse, and the parameter  $f_R = 0.18$  and function

$$h_R(\tau > 0) = (\tau_1^2 + \tau_2^2)/(\tau_1\tau_2^2) \times e^{-\tau/\tau_2} \sin \tau/\tau_1 \quad (\text{A.13})$$

describe the medium's Raman response, with  $\tau_1 = 12.2 \text{ fs}$  and  $\tau_2 = 32 \text{ fs}$  used here [17, 89, 93].

The linear frequency-domain operator applied in the RK4IP algorithm is

$$\hat{L} = i\frac{\beta_2}{2}(\omega_\mu - \omega_0)^2 - \frac{\beta_3}{6}(\omega_\mu - \omega_0)^3 \quad (\text{A.14})$$

Here  $\omega_\mu$  is defined by the discretization of the frequency domain due to Fourier-transformation of a finite temporal window of length  $T_{comp}$  via  $\omega_\mu = \omega_0 + 2\pi\mu/T_{comp}$ ; where  $T_{comp}$  is the size of the domain for the fast time variable  $T$ .

The nonlinear operator  $\hat{N}$  for the GNLSE implements the convolution as a product in the frequency domain. That is,

$$\hat{N} = i\gamma \frac{1}{A} \left( 1 + \frac{1}{\omega_0} \frac{\partial}{\partial T} \right) \times \left[ (1 - f_R)A|A|^2 + f_RA \mathcal{F}^{-1} \{ \chi_R \cdot \mathcal{F}(|A|^2) \} \right], \quad (\text{A.15})$$

where  $\chi_R = \mathcal{F}\{h_R(\tau)\}$  and  $\mathcal{F}$  denotes Fourier transformation. Procedurally, the quantity in the square brackets is calculated first, and then the fast-time derivative is implemented and the sum in the curved brackets is calculated.

## References

- [1] P Del’Haye, A Schliesser, O Arcizet, T Wilken, R Holzwarth, and T. J. Kippenberg. Optical frequency comb generation from a monolithic microresonator. *Nature*, 450 (7173), **2007**, 1214–1217. DOI: 10.1038/nature06401.
- [2] T. J. Kippenberg, R Holzwarth, and S. A. Diddams. Microresonator-Based Optical Frequency Combs. *Science (New York, N.Y.)*, 332 (6029), **2011**, 555–559. DOI: 10.1126/science.1193968.
- [3] A. A. Savchenkov, A. B. Matsko, and L Maleki. On Frequency Combs in Monolithic Resonators. *Nanophotonics*, 5, **2016**, 363–391. DOI: 10.1515/nanoph-2016-0031.
- [4] Y. K. Chembo. Kerr optical frequency combs: Theory, applications and perspectives. *Nanophotonics*, 5 (2), **2016**, 214–230. DOI: 10.1515/nanoph-2016-0013.
- [5] A. Pasquazi, M. Peccianti, L. Razzari, D. J. Moss, S. Coen, M. Erkintalo, Y. K. Chembo, T. Hansson, S. Wabnitz, P. Del’Haye, X. Xue, A. M. Weiner, and R. Morandotti. Micro-combs: A novel generation of optical sources. *Physics Reports*, 729, **2017**, 1–81. DOI: 10.1016/j.physrep.2017.08.004.
- [6] H. Lee, T. Chen, J. Li, K. Y. Yang, S. Jeon, O. Painter, and K. J. Vahala. Chemically etched ultrahigh-Q wedge-resonator on a silicon chip. *Nature Photonics*, 6 (6), **2012**, 369–373. DOI: 10.1038/nphoton.2012.109. arXiv: 1112.2196 (cited on pages 1, 3).
- [7] X. Yi, Q.-F. Yang, K. Y. Yang, M.-G. Suh, and K. Vahala. Soliton frequency comb at microwave rates in a high-Q silica microresonator. *Optica*, 2 (12), **2015**, 1078–1085 (cited on pages 1, 25).
- [8] P. Del’Haye, S. A. Diddams, and S. B. Papp. Laser-machined ultra-high-Q microrod resonators for nonlinear optics. *Applied Physics Letters*, 102, **2013**, 221119 (cited on pages 1, 4).
- [9] W Liang, A. A. Savchenkov, A. B. Matsko, V. S. Ilchenko, D Seidel, and L Maleki. Generation of near-infrared frequency combs from a MgF<sub>2</sub> whispering gallery mode resonator. *Optics Letters*, 36 (12), **2011**, 2290–2292. DOI: 10.1364/OL.36.002290.
- [10] A. a. Savchenkov, A. B. Matsko, V. S. Ilchenko, I. Solomatine, D. Seidel, and L. Maleki. Tunable optical frequency comb with a crystalline whispering gallery mode resonator. *Physical Review Letters*, 101 (9), **2008**, 1–4. DOI: 10.1103/PhysRevLett.101.093902. arXiv: 0804.0263.
- [11] Y. Okawachi, K. Saha, J. S. Levy, Y. H. Wen, M. Lipson, and A. L. Gaeta. Octave-spanning frequency comb generation in a silicon nitride chip. *Optics Letters*, 36 (17), **2011**, 3398–3400. DOI: 10.1364/OL.36.003398. arXiv: 1107.5555.

- [12] D. J. Moss, R. Morandotti, A. L. Gaeta, and M. Lipson. New CMOS-compatible platforms based on silicon nitride and Hydex for nonlinear optics. *Nature Photonics*, 7 (July), **2013**, 597–607. DOI: 10.1038/nphoton.2013.183.
- [13] D. Braje, L. Hollberg, and S. Diddams. Brillouin-Enhanced Hyperparametric Generation of an Optical Frequency Comb in a Monolithic Highly Nonlinear Fiber Cavity Pumped by a cw Laser. *Physical Review Letters*, 102 (19), **2009**, 193902. DOI: 10.1103/PhysRevLett.102.193902.
- [14] E. Obrzud, S. Lecomte, and T. Herr. Temporal solitons in microresonators driven by optical pulses. *Nature Photonics*, 11 (August), **2017**, 600–607. DOI: 10.1038/nphoton.2017.140. arXiv: 1612.08993 (cited on pages 2, 25).
- [15] V. S. Ilchenko and A. B. Matsko. Optical resonators with whispering-gallery modes - Part II: Applications. *IEEE Journal on Selected Topics in Quantum Electronics*, 12 (1), **2006**, 15–32. DOI: 10.1109/JSTQE.2005.862943.
- [16] K. Y. Yang, K. Beha, D. C. Cole, X. Yi, P. Del’Haye, H. Lee, J. Li, D. Y. Oh, S. A. Diddams, S. B. Papp, and K. J. Vahala. Broadband dispersion-engineered microresonator on a chip. *Nature Photonics*, 10 (March), **2016**, 316–320. DOI: 10.1038/nphoton.2016.36.
- [17] G. P. Agrawal. **Nonlinear Fiber Optics**. 4th. Burlington, MA: Elsevier, 2007 (cited on pages 3, 9, 10, 12, 19, 20, 38, 46).
- [18] M. L. Calvo and V. Lakshminarayanan, eds. **Optical Waveguides: From Theory to Applied Technologies**. Boca Raton, FL: Taylor & Francis, 2007.
- [19] A. N. Oraevsky. Whispering-gallery waves. *Quantum Electronics*, 32 (42), **2002**, 377–400. DOI: 10.1070/QE2001v031n05ABEH002205. arXiv: arXiv:1011.1669v3.
- [20] H. A. Haus. **Waves and Fields in Optoelectronics**. Englewood Cliffs: Prentice-Hall, 1984.
- [21] J. C. Knight, G. Cheung, F. Jacques, and T. A. Birks. Phase-matched excitation of whispering-gallery-mode resonances by a fiber taper. *Optics Letters*, 22 (15), **1997**, 1129. DOI: 10.1364/OL.22.001129.
- [22] S. M. Spillane, T. J. Kippenberg, O. J. Painter, and K. J. Vahala. Ideality in a Fiber-Taper-Coupled Microresonator System for Application to Cavity Quantum Electrodynamics. *Physical review letters*, 91 (4), **2003**, 043902. DOI: 10.1103/PhysRevLett.91.043902.
- [23] E. Shah Hosseini, S. Yegnanarayanan, A. H. Atabaki, M. Soltani, and A. Adibi. Systematic design and fabrication of high-Q single-mode pulley-coupled planar silicon nitride microdisk resonators at visible wavelengths. *Optics Express*, 18 (3), **2010**, 2127. DOI: 10.1364/OE.18.002127.
- [24] T. Carmon, L. Yang, and K. J. Vahala. Dynamical thermal behavior and thermal self-stability of microcavities. *Optics Express*, 12 (20), **2004**, 4742–4750. URL: <http://www.ncbi.nlm.nih.gov/pubmed/19484026><http://www.opticsinfobase.org/oe/abstract.cfm?uri=oe-12-20-4742>.
- [25] R. W. Boyd. **Nonlinear Optics**. San Diego, CA: Elsevier, 2003.

- [26] R. del Coso and J. Solis. Relation between nonlinear refractive index and third-order susceptibility in absorbing media. *Journal of the Optical Society of America B*, 21 (3), **2004**, 640. DOI: 10.1364/JOSAB.21.000640.
- [27] T. Kippenberg, S. Spillane, and K. Vahala. Kerr-Nonlinearity Optical Parametric Oscillation in an Ultrahigh-Q Toroid Microcavity. *Physical Review Letters*, 93 (8), **2004**, 083904. DOI: 10.1103/PhysRevLett.93.083904.
- [28] A. A. Savchenkov, A. B. Matsko, D. Strekalov, M. Mohageg, V. S. Ilchenko, and L. Maleki. Low threshold optical oscillations in a whispering gallery mode CaF<sub>2</sub> resonator. *Physical Review Letters*, 93 (24), **2004**, 2–5. DOI: 10.1103/PhysRevLett.93.243905.
- [29] I. H. Agha, Y. Okawachi, M. A. Foster, J. E. Sharping, and A. L. Gaeta. Four-wave-mixing parametric oscillations in dispersion-compensated high-Q silica microspheres. *Physical Review A - Atomic, Molecular, and Optical Physics*, 76 (4), **2007**, 1–4. DOI: 10.1103/PhysRevA.76.043837.
- [30] T. Herr, V. Brasch, J. D. Jost, C. Y. Wang, N. M. Kondratiev, M. L. Gorodetsky, and T. J. Kippenberg. Temporal solitons in optical microresonators. *arXiv*, **2012**, 1211.0733. DOI: 10.1038/nphoton.2013.343. arXiv: 1211.0733.
- [31] T. Herr, V. Brasch, J. D. Jost, C. Y. Wang, N. M. Kondratiev, M. L. Gorodetsky, and T. J. Kippenberg. Temporal solitons in optical microresonators. *Nature Photonics*, 8 (2), **2014**, 145–152. DOI: 10.1109/CLEOE-IQEC.2013.6801769. arXiv: 1211.0733 (cited on pages 10, 12, 22, 23, 25).
- [32] F. Leo, S. Coen, P. Kockaert, S.-P. Gorza, P. Emplit, and M. Haelterman. Temporal cavity solitons in one-dimensional Kerr media as bits in an all-optical buffer. *Nature Photonics*, 4 (7), **2010**, 471–476. DOI: 10.1038/nphoton.2010.120.
- [33] T. Herr, K. Hartinger, J. Riemensberger, C. Y. Wang, E. Gavartin, R. Holzwarth, M. L. Gorodetsky, and T. J. Kippenberg. Universal formation dynamics and noise of Kerr-frequency combs in microresonators. *Nature Photonics*, 6 (7), **2012**, 480–487. DOI: 10.1038/nphoton.2012.127.
- [34] Y. K. Chembo and C. R. Menyuk. Spatiotemporal Lugiato-Lefever formalism for Kerr-comb generation in whispering-gallery-mode resonators. *Physical Review A*, 87, **2013**, 053852. DOI: 10.1103/PhysRevA.87.053852.
- [35] S. Coen, H. G. Randle, T. Sylvestre, and M. Erkintalo. Modeling of octave-spanning Kerr frequency combs using a generalized mean-field Lugiato-Lefever model. *Optics letters*, 38 (1), **2013**, 37–39. URL: <http://www.ncbi.nlm.nih.gov/pubmed/23282830>.
- [36] M. Haelterman, S. Trillo, and S. Wabnitz. Dissipative modulation instability in a nonlinear dispersive ring cavity. *Optics Communications*, 91 (5-6), **1992**, 401–407. DOI: 10.1016/0030-4018(92)90367-Z.
- [37] T. Hansson, M. Bernard, and S. Wabnitz. Modulational Instability of Nonlinear Polarization Mode Coupling in Microresonators. 35 (4), **2018**. URL: <https://arxiv.org/pdf/1802.04535.pdf>. arXiv: arXiv:1802.04535v1.

- [38] Y. K. Chembo, I. S. Grudinin, and N Yu. Spatiotemporal dynamics of Kerr-Raman optical frequency combs. *Physical Review A*, 92 (4), **2015**, 4. DOI: 10.1103/PhysRevA.92.043818.
- [39] C. Godey, I. V. Balakireva, A. Coillet, and Y. K. Chembo. Stability analysis of the spatiotemporal Lugiato-Lefever model for Kerr optical frequency combs in the anomalous and normal dispersion regimes. *Physical Review A*, 89 (6), **2014**, 063814. DOI: 10.1103/PhysRevA.89.063814.
- [40] I. V. Barashenkov and Y. S. Smirnov. Existence and stability chart for the ac-driven, damped nonlinear Schrödinger solitons. *Physical Review E - Statistical Physics, Plasmas, Fluids, and Related Interdisciplinary Topics*, 54 (5), **1996**, 5707–5725. DOI: 10.1103/PhysRevE.54.5707.
- [41] A Coillet and Y. K. Chembo. Routes to spatiotemporal chaos in Kerr optical frequency combs. *Chaos*, 24 (1), **2014**, 5. DOI: 10.1063/1.4863298. arXiv: arXiv:1401.0927v1.
- [42] L. A. Lugiato and R Lefever. Spatial Dissipative Structures in Passive Optical Systems. *Physical Review Letters*, 58 (21), **1987**, 2209–2211.
- [43] L. Lugiato and R Lefever. Diffraction stationary patterns in passive optical systems. *Interaction of Radiation with Matter*, **1987**.
- [44] W. H. Renninger and P. T. Rakich. Closed-form solutions and scaling laws for Kerr frequency combs. *Scientific Reports*, 6 (1), **2016**, 24742. DOI: 10.1038/srep24742. arXiv: 1412.4164.
- [45] J. S. Russell. Report on Waves. *Fourteenth meeting of the British Association for the Advancement of Science*, **1844**, 311–390.
- [46] M. Brambilla, L. A. Lugiato, F. Prati, L. Spinelli, and W. J. Firth. Spatial soliton pixels in semiconductor devices. *Physical Review Letters*, 79 (11), **1997**, 2042–2045. DOI: 10.1103/PhysRevLett.79.2042.
- [47] S. Minardi, F. Eilenberger, Y. V. Kartashov, A. Szameit, U. Röpke, J. Kobelke, K. Schuster, H. Bartelt, S. Nolte, L. Torner, F. Lederer, A. Tünnermann, and T. Pertsch. Three-dimensional light bullets in arrays of waveguides. *Physical Review Letters*, 105 (26), **2010**, 1–4. DOI: 10.1103/PhysRevLett.105.263901. arXiv: 1101.0734.
- [48] F. X. Kärtner, I. D. Jung, and U. Keller. Soliton mode-locking with saturable absorbers. *IEEE Journal on Selected Topics in Quantum Electronics*, 2 (3), **1996**, 540–556. DOI: 10.1109/2944.571754.
- [49] P. Grelu and N. Akhmediev. Dissipative solitons for mode-locked lasers. *Nature Photonics*, 6 (February), **2012**, 84–92. DOI: 10.1109/PGC.2010.5706017.
- [50] L. F. Mollenauer and J. P. Gordon. **Solitons in Optical Fibers**. Academic Press, 2006, p. 296.
- [51] A. Hasegawa and Y. Kodama. **Solitons in Optical Communications**. Academic Press, 1995.
- [52] H. A. Haus and W. S. Wong. Solitons in optical communications. *Reviews of Modern Physics*, 68 (2), **1996**, 423–444. DOI: 10.1103/RevModPhys.68.423.
- [53] S. Coen and M. Erkintalo. Universal scaling laws of Kerr frequency combs. *Optics letters*, 38 (11), **2013**, 1790–1792. DOI: 10.1364/OL.38.001790. arXiv: arXiv:1303.7078v1.



- [54] H. Guo, M. Karpov, E. Lucas, A. Kordts, M. H. Pfeiffer, V. Brasch, G. Lihachev, V. E. Lobanov, M. L. Gorodetsky, and T. J. Kippenberg. Universal dynamics and deterministic switching of dissipative Kerr solitons in optical microresonators. *Nature Physics*, 13 (1), **2017**, 94–102. DOI: 10.1038/nphys3893. arXiv: 1601.05036.
- [55] N. J. Zabusky and M. D. Kruskal. Interaction of "solitons" in a collisionless plasma and the recurrence of initial states. *Physical Review Letters*, 15 (6), **1965**, 240.
- [56] J. P. Gordon. Interaction forces among solitons in optical fibers. *Optics Letters*, 8 (11), **1983**, 596. DOI: 10.1364/OL.8.000596.
- [57] B. A. Malomed. Bound solitons in the nonlinear Schrodinger-Ginzburg-Landau equation. *Physical Review A*, 44 (10), **1991**, 6954–6957. DOI: 10.1103/PhysRevA.44.6954.
- [58] J. K. Jang, M. Erkintalo, S. G. Murdoch, and S. Coen. Ultraweak long-range interactions of solitons observed over astronomical distances. *Nature Photonics*, 7 (8), **2013**, 657–663. DOI: 10.1038/nphoton.2013.157. arXiv: arXiv:1305.6670v1.
- [59] P. Parra-Rivas, D. Gomila, P. Colet, and L. Gelens. Interaction of solitons and the formation of bound states in the generalized Lugiato-Lefever equation. *European Physical Journal D*, 71 (7), **2017**, 198. DOI: 10.1140/epjd/e2017-80127-5. arXiv: arXiv:1705.02619v1 (cited on page 23).
- [60] Y. Wang, F. Leo, J. Fatome, M. Erkintalo, S. G. Murdoch, and S. Coen. Universal mechanism for the binding of temporal cavity solitons, **2017**, 1–10. URL: <http://arxiv.org/abs/1703.10604>. arXiv: 1703.10604 (cited on page 23).
- [61] V. Brasch, T. Herr, M. Geiselmann, G. Lihachev, M. H. P. Pfeiffer, M. L. Gorodetsky, and T. J. Kippenberg. Photonic chip-based optical frequency comb using soliton Cherenkov radiation. *Science*, 351 (6271), **2016**, 357. DOI: 10.1364/CLEO\_SI.2015.STh4N.1. arXiv: 1410.8598.
- [62] J. R. Stone, T. C. Briles, T. E. Drake, D. T. Spencer, D. R. Carlson, S. A. Diddams, and S. B. Papp. Thermal and Nonlinear Dissipative-Soliton Dynamics in Kerr Microresonator Frequency Combs. *arXiv*, **2017**, 1708.08405. URL: <http://arxiv.org/abs/1708.08405>. arXiv: 1708.08405 (cited on page 25).
- [63] V. E. Lobanov, G. V. Lihachev, N. G. Pavlov, A. V. Cherenkov, T. J. Kippenberg, and M. L. Gorodetsky. Harmonization of chaos into a soliton in Kerr frequency combs. *Optics Express*, 24 (24), **2016**, 27382. DOI: 10.1126/science.aah4243. arXiv: 1607.08222 (cited on page 25).
- [64] C. Joshi, J. K. Jang, K. Luke, X. Ji, S. A. Miller, A. Klenner, Y. Okawachi, M. Lipson, and A. L. Gaeta. Thermally controlled comb generation and soliton modelocking in microresonators. *Optics Letters*, 41 (11), **2016**, 2565–2568. DOI: 10.1364/OL.41.002565. arXiv: 1603.08017.
- [65] W. Wang, Z. Lu, W. Zhang, S. T. Chu, B. E. Little, L. Wang, X. Xie, M. Liu, Q. Yang, L. Wang, J. Zhao, G. Wang, Q. Sun, Y. Liu, Y. Wang, and W. Zhao. Robust soliton crystals in a thermally controlled microresonator. *Optics Letters*, 43 (9), **2018**, 2002–2005. DOI: 10.1364/OL.43.002002.

- [66] J. K. Jang, M. Erkintalo, S. G. Murdoch, and S. Coen. Writing and erasing of temporal cavity solitons by direct phase modulation of the cavity driving field. *Optics Letters*, 40 (20), **2015**, 4755–4758. DOI: 10.1364/OL.40.004755. arXiv: 1501.05289 (cited on page 25).
- [67] J. K. Jang, M. Erkintalo, S. Coen, and S. G. Murdoch. Temporal tweezing of light through the trapping and manipulation of temporal cavity solitons. *Nature Communications*, 6, **2015**, 7370. DOI: 10.1038/ncomms8370. arXiv: 1410.4836 (cited on page 25).
- [68] Y. Wang, B. Garbin, F. Leo, S. Coen, M. Erkintalo, and S. G. Murdoch. Writing and Erasure of Temporal Cavity Solitons via Intensity Modulation of the Cavity Driving Field. *arXiv*, **2018**, 1802.07428. arXiv: 1802.07428 (cited on page 25).
- [69] S. B. Papp, K. Beha, P. Del’Haye, F. Quinlan, H. Lee, K. J. Vahala, and S. A. Diddams. Microresonator frequency comb optical clock. *Optica*, 1 (1), **2014**, 10–14. DOI: 10.1364/OPTICA.1.000010. arXiv: 1309.3525.
- [70] M. G. Suh, Q. F. Yang, K. Y. Yang, X. Yi, and K. J. Vahala. Microresonator soliton dual-comb spectroscopy. *Science*, 354 (6312), **2016**, 1–5. DOI: 10.1126/science.aah6516. arXiv: 1607.08222.
- [71] P. Marin-Palomo, J. N. Kemal, M. Karpov, A. Kordts, J. Pfeifle, M. H. Pfeiffer, P. Trocha, S. Wolf, V. Brasch, M. H. Anderson, R. Rosenberger, K. Vijayan, W. Freude, T. J. Kippenberg, and C. Koos. Microresonator-based solitons for massively parallel coherent optical communications. *Nature*, 546 (7657), **2017**, 274–279. DOI: 10.1038/nature22387. arXiv: 1610.01484.
- [72] D. T. Spencer, T. Drake, T. C. Briles, J. Stone, L. C. Sinclair, C. Fredrick, Q. Li, D. Westly, B. R. Ilic, A. Bluestone, N. Volet, T. Komljenovic, L. Chang, S. H. Lee, D. Y. Oh, T. J. Kippenberg, E. Norberg, L. Theogarajan, M.-g. Suh, K. Y. Yang, H. P. Martin, K. Vahala, N. R. Newbury, K. Srinivasan, J. E. Bowers, S. A. Diddams, and S. B. Papp. An optical-frequency synthesizer using integrated photonics. *Nature*, 557, **2018**, 81–85. DOI: 10.1038/s41586-018-0065-7.
- [73] J. D. Jost, T. Herr, C. Lecaplain, V. Brasch, M. H. P. Pfeiffer, and T. J. Kippenberg. Counting the cycles of light using a self-referenced optical microresonator. *Optica*, 2 (8), **2015**, 706–711. DOI: 10.1364/OPTICA.2.000706. arXiv: 1411.1354.
- [74] P. Del’Haye, A. Coillet, T. Fortier, K. Beha, D. C. Cole, K. Y. Yang, H. Lee, K. J. Vahala, S. B. Papp, and S. A. Diddams. Phase-coherent microwave-to-optical link with a self-referenced microcomb. *Nature Photonics*, 10 (June), **2016**, 1–5. DOI: 10.1038/nphoton.2016.105.
- [75] V. Brasch, E. Lucas, J. D. Jost, M. Geiselmann, and T. J. Kippenberg. Self-referenced photonic chip soliton Kerr frequency comb. *Light: Science & Applications*, 6 (1), **2017**, e16202. DOI: 10.1038/lsa.2016.202. arXiv: 1605.02801.
- [76] T. C. Briles, J. R. Stone, T. E. Drake, D. T. Spencer, C. Frederick, Q. Li, D. A. Westly, B. R. Ilic, K. Srinivasan, S. A. Diddams, and S. B. Papp. Kerr-microresonator solitons for accurate carrier-envelope-frequency stabilization. *arXiv*, **2017**, 1711.06251. URL: <http://arxiv.org/abs/1711.06251>. arXiv: 1711.06251.

- [77] S. Backus, C. G. Durfee, M. M. Murnane, and H. C. Kapteyn. High power ultrafast lasers. *Review of Scientific Instruments*, 69 (3), **1998**, 1207. DOI: 10.1063/1.1148795.
- [78] A. Baltuska, M. Uiberacker, E. Goulielmakis, R. Kienberger, V. S. Yakovlev, T. Udem, T. W. Hänsch, and F. Krausz. Phase-Controlled Amplification of Few-Cycle Laser Pulses. *IEEE Journal of Selected Topics in Quantum Electronics*, 9 (4), **2003**, 972–989.
- [79] C. Gohle, J. Rauschenberger, T. Fuji, T. Udem, A. Apolonski, F. Krausz, and T. W. Hänsch. Carrier envelope phase noise in stabilized amplifier systems. 30 (18), **2005**, 2487–2489.
- [80] J. Rauschenberger, T. Fuji, M. Hentschel, A.-J. Verhoef, T. Udem, C. Gohle, T. W. Hänsch, and F. Krausz. Carrier-envelope phase-stabilized amplifier system. *Laser Physics Letters*, 3 (1), **2006**, 37–42. DOI: 10.1002/lapl.200510053.
- [81] M. E. Fermann, V. I. Kruglov, B. C. Thomsen, J. M. Dudley, and J. D. Harvey. Self-similar propagation and amplification of parabolic pulses in optical fibers. *Physical review letters*, 84 (26 Pt 1), **2000**, 6010–3. URL: <http://www.ncbi.nlm.nih.gov/pubmed/10991111>.
- [82] M. Hirano, T. Nakanishi, T. Okuno, and M. Onishi. Silica-Based Highly Nonlinear Fibers and Their Application. *Sel. Top. Quantum Electron.*, 15 (1), **2009**, 103–113. DOI: 10.1109/JSTQE.2008.2010241 (cited on pages 29, 46).
- [83] D. Mandridis, I. Ozdur, F. Quinlan, M. Akbulut, J. J. Plant, P. W. Juodawlkis, and P. J. Delfyett. Low-noise, low repetition rate, semiconductor-based mode-locked laser source suitable for high bandwidth photonic analog digital conversion. *Applied Optics*, 49 (15), **2010**, 2850–2857.
- [84] J. M. Dudley, G. G. Genty, and S. Coen. Supercontinuum generation in photonic crystal fiber. *Reviews of Modern Physics*, 78 (4), **2006**, 1135–1184. DOI: 10.1103/RevModPhys.78.1135.
- [85] H.-A. Bachor and P. J. Manson. Practical Implications of Quantum Noise. *Journal of Modern Optics*, 37 (11), **1990**, 1727–1740. DOI: 10.1080/09500349014551951.
- [86] F. Quinlan, T. M. Fortier, H. Jiang, and S. a. Diddams. Analysis of shot noise in the detection of ultrashort optical pulse trains. *Journal of the Optical Society of America B*, 30 (6), **2013**, 1775. DOI: 10.1364/JOSAB.30.001775.
- [87] D. C. Cole, K. M. Beha, S. A. Diddams, and S. B. Papp. Octave-spanning supercontinuum generation via microwave frequency multiplication. *Proceedings of the 8th Symposium on Frequency Standards and Metrology 2015, Journal of Physics: Conference Series*, 723, **2016**, 012035. DOI: 10.1088/1742-6596/723/1/012035.
- [88] A. M. Heidt. Efficient Adaptive Step Size Method for the Simulation of Supercontinuum Generation in Optical Fibers. *Journal of Lightwave Technology*, 27 (18), **2009**, 3984–3991 (cited on pages 38, 42, 43).
- [89] J. Hult. A Fourth-Order Runge-Kutta in the Interaction Picture Method for Simulating Supercontinuum Generation in Optical Fibers. *Journal of Lightwave Technology*, 25 (12), **2007**, 3770–3775. DOI: 10.1109/JLT.2007.909373 (cited on pages 38, 42, 43, 46).

- [90] K. Beha, D. C. Cole, P. Del’Haye, A. Coillet, S. A. Diddams, and S. B. Papp. Electronic synthesis of light. *Optica*, 4 (4), **2017**, 406–411. DOI: 10.1364/OPTICA.4.000406.
- [91] R. Driad, J. Rosenzweig, R. E. Makon, R. Lösch, V. Hurm, H. Walcher, and M. Schlechtweg. InP DHBT-Based IC Technology for 100-Gb / s Ethernet. *IEEE Trans. on Electron. Devices*, 58 (8), **2011**, 2604–2609.
- [92] D. Ferenci, M. Grozing, M. Berroth, R. Makon, R. Driad, and J. Rosenzweig. A 25 GHz Analog Demultiplexer with a Novel Track and Hold Circuit for a 50 GS / s A / D-Conversion System in InP DHBT Technology. In: **Microwave Symposium Digest**. 2012, pp. 1–3.
- [93] K. J. Blow and D Wood. Theoretical description of transient stimulated Raman scattering in optical fibers. *Quantum Electronics, IEEE Journal of*, 25 (12), **1989**, 2665–2673. DOI: 10.1109/3.40655 (cited on page 46).